

REPORT DOCUMENTATION PAGE

Form Approved OMB NO. 0704-0188

The public reporting burden for this collection of information is estimated to average 1 hour per response, including the time for reviewing instructions, searching existing data sources, gathering and maintaining the data needed, and completing and reviewing the collection of information. Send comments regarding this burden estimate or any other aspect of this collection of information, including suggestions for reducing this burden, to Washington Headquarters Services, Directorate for Information Operations and Reports, 1215 Jefferson Davis Highway, Suite 1204, Arlington VA, 22202-4302. Respondents should be aware that notwithstanding any other provision of law, no person shall be subject to any penalty for failing to comply with a collection of information if it does not display a currently valid OMB control number.

PLEASE DO NOT RETURN YOUR FORM TO THE ABOVE ADDRESS.

1. REPORT DATE (DD-MM-YYYY) 28-06-2015	2. REPORT TYPE Final Report	3. DATES COVERED (From - To) 1-May-2010 - 30-Apr-2014		
4. TITLE AND SUBTITLE Final Report: Saturated Particle Transport in Porous Media: An Investigation into the Influence of Flow Direction and Particle Size Distribution		5a. CONTRACT NUMBER W911NF-10-1-0123		
		5b. GRANT NUMBER		
		5c. PROGRAM ELEMENT NUMBER 611102		
6. AUTHORS Patricia J. Culligan		5d. PROJECT NUMBER		
		5e. TASK NUMBER		
		5f. WORK UNIT NUMBER		
7. PERFORMING ORGANIZATION NAMES AND ADDRESSES Columbia University 615 West 131st Street Mail Code 8725 New York, NY 10027 -6902		8. PERFORMING ORGANIZATION REPORT NUMBER		
9. SPONSORING/MONITORING AGENCY NAME(S) AND ADDRESS (ES) U.S. Army Research Office P.O. Box 12211 Research Triangle Park, NC 27709-2211		10. SPONSOR/MONITOR'S ACRONYM(S) ARO		
		11. SPONSOR/MONITOR'S REPORT NUMBER(S) 55094-EV.4		
12. DISTRIBUTION AVAILABILITY STATEMENT Approved for Public Release; Distribution Unlimited				
13. SUPPLEMENTARY NOTES The views, opinions and/or findings contained in this report are those of the author(s) and should not be construed as an official Department of the Army position, policy or decision, unless so designated by other documentation.				
14. ABSTRACT The real-time spatial resolution of 1-?m fluorescent particles, 3-?m, 6-?m, 1-25-?m mixed particles, and 1-?m with 6-?m particles present, and 6-?m with 1-?m particles present, were determined under one-dimensional, steady state flow conditions through saturated beds of rough glass beads under different flow directions. A kinetic particle transport model was developed, which assumed both reversible and irreversible particle attachment, and accounted for a dual particle population. The model was fitted to the experimental results to quantify the influence of flow direction and initial size distribution on mean local attachment kinetics. The results confirm the hypothesis that				
15. SUBJECT TERMS Porous Media, Colloid Transport, Flow Direction				
16. SECURITY CLASSIFICATION OF: a. REPORT UU		17. LIMITATION OF ABSTRACT UU	15. NUMBER OF PAGES	19a. NAME OF RESPONSIBLE PERSON Patricia Culligan
b. ABSTRACT UU		c. THIS PAGE UU		19b. TELEPHONE NUMBER 212-854-3154

Report Title

Final Report: Saturated Particle Transport in Porous Media: An Investigation into the Influence of Flow Direction and Particle Size Distribution

ABSTRACT

The real-time spatial resolution of 1-?m fluorescent particles, 3-?m, 6-?m, 1-25-?m mixed particles, and 1-?m with 6-?m particles present, and 6-?m with 1-?m particles present, were determined under one-dimensional, steady state flow conditions through saturated beds of rough glass beads under different flow directions. A kinetic particle transport model was developed, which assumed both reversible and irreversible particle attachment, and accounted for a dual particle population. The model was fitted to the experimental results to quantify the influence of flow direction and particle size distribution on macro-scale attachment kinetics. The results confirm the hypothesis that particle attachment kinetics is influenced by flow direction, as well as particle size. To explore particle attachment kinetics at the micro-scale, the Fluent software was used to generate a velocity distribution field in the vicinity of rough-walled collector and a Fortran code was written to carry out microscopic particle tracking under two-dimensional, steady-state flow conditions. The results of the particle tracking simulations also confirmed that particle attachment mechanisms at the micro-scale vary with flow direction and particle size. Overall, the research indicates the need for sophisticated particle fate and transport models in order to capture the physics of particle transport under realistic, three-dimensional transport conditions.

Enter List of papers submitted or published that acknowledge ARO support from the start of the project to the date of this printing. List the papers, including journal references, in the following categories:

(a) Papers published in peer-reviewed journals (N/A for none)

Received Paper

04/27/2015 1.00 P.S.K. Knappett, J. Du, P. Liu, V. Horvath, B.J. Mailloux, J. Feighery, A. van Geen, P.J. Culligan.
Importance of reversible attachment in predicting *E. coli* transport in saturated aquifers from column experiments,
Advances in Water Resources, (01 2014): 120. doi: 10.1016/j.advwatres.2013.11.005

TOTAL: **1**

Number of Papers published in peer-reviewed journals:

(b) Papers published in non-peer-reviewed journals (N/A for none)

Received Paper

TOTAL:

Number of Papers published in non peer-reviewed journals:

(c) Presentations

American Geophysical Union Fall Meeting 2011, 5- 9th December, San Francisco California, 2011: Poster Presentation: The Influence of Flow Direction and Particle Size Distribution on Particle Attachment.

Number of Presentations: 1.00

Non Peer-Reviewed Conference Proceeding publications (other than abstracts):

Received Paper

TOTAL:

Number of Non Peer-Reviewed Conference Proceeding publications (other than abstracts):

Peer-Reviewed Conference Proceeding publications (other than abstracts):

Received Paper

TOTAL:

Number of Peer-Reviewed Conference Proceeding publications (other than abstracts):

(d) Manuscripts

Received Paper

04/27/2015 2.00 Po-Chieh Liu, Brain Mailloux, John Magyar, Patricia Culligan. Can varying velocity conditions explain differences between laboratory and field observations of bacterial transport in porous media?, To be submitted for publication (04 2015)

04/27/2015 3.00 Adnan Altinors, Patricia Culligan. A TRAJECTORY MODEL FOR EXPLORING PARTICLE RETENTIONIN THE VICINITY OF A COLLECTORWITH AN IRREGULAR SURFACE, Advances in Water Resources (05 2015)

TOTAL: **2**

Number of Manuscripts:

Books

Received Book

TOTAL:

Received Book Chapter

TOTAL:

Patents Submitted

Patents Awarded

Awards

None

Graduate Students

NAME	PERCENT SUPPORTED	Discipline
Po-Chieh Liu	0.80	
John Feighery	0.00	
Jianqing Du	0.00	
FTE Equivalent:	0.80	
Total Number:	3	

Names of Post Doctorates

<u>NAME</u>	<u>PERCENT_SUPPORTED</u>
Adnan Altay Altinors	0.00
Peter Knappett	0.00
Andrew Ferguson	0.50
FTE Equivalent:	0.50
Total Number:	3

Names of Faculty Supported

<u>NAME</u>	<u>PERCENT_SUPPORTED</u>	National Academy Member
Patricia Culligan	0.10	
Brian Mailloux	0.00	
FTE Equivalent:	0.10	
Total Number:	2	

Names of Under Graduate students supported

<u>NAME</u>	<u>PERCENT_SUPPORTED</u>	Discipline
Ashley Wagner	0.00	Environmental Science
Veronica Horvath	0.00	Environmental Science
FTE Equivalent:	0.00	
Total Number:	2	

Student Metrics

This section only applies to graduating undergraduates supported by this agreement in this reporting period

The number of undergraduates funded by this agreement who graduated during this period: 0.00

The number of undergraduates funded by this agreement who graduated during this period with a degree in science, mathematics, engineering, or technology fields:..... 0.00

The number of undergraduates funded by your agreement who graduated during this period and will continue to pursue a graduate or Ph.D. degree in science, mathematics, engineering, or technology fields:..... 0.00

Number of graduating undergraduates who achieved a 3.5 GPA to 4.0 (4.0 max scale):..... 0.00

Number of graduating undergraduates funded by a DoD funded Center of Excellence grant for Education, Research and Engineering:..... 0.00

The number of undergraduates funded by your agreement who graduated during this period and intend to work for the Department of Defense 0.00

The number of undergraduates funded by your agreement who graduated during this period and will receive scholarships or fellowships for further studies in science, mathematics, engineering or technology fields:..... 0.00

Names of Personnel receiving masters degrees

<u>NAME</u>
Jianqing Du
Total Number:

Names of personnel receiving PHDs

<u>NAME</u>
Total Number:

Names of other research staff

<u>NAME</u>	<u>PERCENT SUPPORTED</u>
-------------	--------------------------

 FTE Equivalent: | **Total Number:** |

Sub Contractors (DD882)

Inventions (DD882)

Scientific Progress

See attachment.

Technology Transfer

None

Period Covered: May 01, 2010 and ending April 31, 2014

Title: SATURATED PARTICLE TRANSPORT IN POROUS MEDIA: AN INVESTIGATION
INTO THE INFLUENCE OF FLOW DIRECTION AND PARTICLE SIZE DISTRIBUTION

Grant Number: W911NF-10-1-0123

Authors: P.J. Culligan

Organizations:

Civil Engineering and Engineering Mechanics
COLUMBIA UNIVERSITY
Seeley W. Mudd
500 West 120th Street
New York, NY 10027

ARO Proposal Number: 55094-EV

TABLE OF CONTENTS

Abstract	2
Scientific Progress and Accomplishments	3
Experimental Approach	4
Modeling Approach	6
Accomplishments	8
Figures	16
Tables	56

Abstract: The real-time spatial resolution of 1- μm fluorescent particles, 3- μm , 6- μm , 1-25- μm mixed particles, and 1- μm with 6- μm particles present, and 6- μm with 1- μm particles present, were determined under one-dimensional, steady state flow conditions through saturated beds of rough glass beads under different flow directions. A kinetic particle transport model was developed, which assumed both reversible and irreversible particle attachment, and accounted for a dual particle population. The model was fitted to the experimental results to quantify the influence of flow direction and particle size distribution on macro-scale attachment kinetics. The results confirm the hypothesis that particle attachment kinetics is influenced by flow direction, as well as particle size. To explore particle attachment kinetics at the micro-scale, the Fluent software was used to generate a velocity distribution field in the vicinity of rough-walled collector and a Fortran code was written to carry out microscopic particle tracking under two-dimensional, steady-state flow conditions. The results of the particle tracking simulations also confirmed that particle attachment mechanisms at the micro-scale vary with flow direction and particle size. Overall, the research indicates the need for sophisticated particle fate and transport models in order to capture the physics of particle transport under realistic, three-dimensional transport conditions.

Scientific Progress and Accomplishments

Background and Objectives

Subsurface contamination is present at many U.S. Army installations due to historical military and industrial operations. Contaminants can include PCBs, fuels, solvents, herbicides/pesticides, heavy metals, munitions materials, and radioactive materials. Increasing evidence now exists that such contaminants are transported not only in a dissolved state by mobile groundwater, but also as a sorbed phase on moving particulate matter such as humic substances, clay particles, colloidal silica and metal oxides [*Šimunek et al., 2006a*]. Sound strategies to deal with legacy contamination at U.S. Army installations therefore require knowledge of the severity and extent of contamination, as well as its likely mobility in the subsurface. Furthermore, U.S. Army operations that involve temporary water and sanitation infrastructure also require knowledge of microbial transport processes in the subsurface in order to identify, for example, appropriate latrine set-pack distances.

For the saturated transport of dissolved contaminants, past approaches have invoked solute fate and transport processes to predict contaminant mobility *National Research Council, 1992*]. However, such programs discount the influence of flow direction and particle size distribution in their interpretation of laboratory or field experiments, and have led to the generation of a range of particle filtration and transport models that are thought to be universal but, instead, are only applicable to the specific flow conditions of the observations themselves. The ultimate goal of this work was the generation of new knowledge regarding saturated particle transport in porous media, with a specific focus on explaining the fundamental roles of flow direction and particle size distribution on particle filtration. To meet this objective, particle transport experiments were conducted in the laboratory under a range of flow and particle size conditions and the results of these experiments were used to parameterize macroscopic models of particle transport. In addition, microscopic modeling based on particle tracking was used to explore fundamental mechanisms for particle fate and transport at the micro-scale.

National Research Council, (1992), Review of Ground Water Modeling Needs for the U.S. Army, National Academy Press, Washington, D.C.

Šimunek, J., C. He, L. Pang, and S.A. Bradford (2006a), Colloid-Facilitated Solute Transport in Variably Saturated Porous Media: Numerical Model and Experimental Verification, Vadose Zone J 5:1035-1047

EXPERIMENTAL APPROACH

Column Experiments

Butyrate plastic core liners (1.7 cm ID) were used to make 12 cm long columns. Core liner end caps were modified with a polypropylene hose nipple (Luer Lock fittings) to allow flow into and out of the columns. Column fill material (collector matrix) consisted of rough glass beads (0.5 mm) which prior to use were washed in distilled water, ultrasonicated and dried over night at 80 deg C. All column experiments involved one-dimensional, steady-state flow conditions. Columns were wet packed and average volumetric porosity was 0.38. A multi-channel peristaltic pump (Gilson Minipuls 3) was used to introduce test solutions into the column at a pore fluid velocity of 1.7 m/d. Flow direction was upward, downward or horizontal. Tubing consisted of inert 0.8 mm ID tubing (Masterflex BioPharm platinumcured L/S 13, Fisher Scientific). Column effluent samples were collected in 15 ml polypropylene tubes using a fraction collector (LKB-Bromma, Sweden). Figure 1 provides a schematic of the experimental set-up.

The inlet particle solution contained 1- μ m carboxylated polystyrene Glacial Blue microspheres (Bangs Laboratories, Fishers, IN) at a final concentration of 0.5 mg/L in distilled water. Distilled water containing no microspheres was used for the particle flush. The pH of both solutions was adjusted to 7.5. Modification of the ionic strength involved the addition of sufficient KBr and KCl (particle solution) or KCl (particle flush solution) to achieve a working concentration of 3.5 mM or 20 mM. All solutions were agitated throughout the experiments with samples of the particle and flush solutions taken before and after an experiment to verify constant conditions.

The protocol for column experiments consisted of:

- Wet packing of the column with glass beads
- Flushing with approximately 5 pore volumes (PV) of the particle-free solution
- 10 PV of particle injection (particles + conservative tracer KBr)
- 10 PV of particle flushing
- Monitoring of breakthrough curve
- Destructive sectioning of the column.

Rectangular box experiments

Real-time spatial resolution of particle concentrations took place in an acrylic box having interior dimensions 14(h) x 3.5(w) x 1(d) cm, Figure 2. The inside walls of the box were lined by thin glass plates to prevent particle attachment to the walls. A void space created at the base of the box enabled monitoring of particle breakthrough curves during downward flow experiments.

Box fill material (collector matrix) consisted of rough glass beads (0.5 mm) that, prior to use, were washed in distilled water, ultrasonicated and dried over night at 50°C. The glass beads were uniformly deposited in 2 cm high layers to a final height of approximately 10 cm and an average volumetric porosity of 0.38. All column experiments involved one-dimensional, steady-state flow at a pore fluid velocity of 2×10^{-3} cm/s using a multi-channel peristaltic pump (Gilson Minipuls 3). Tubing consisted of inert 0.8 mm ID tubing (Masterflex BioPharm platinum-cured L/S 13, Fisher Scientific). Column effluent samples were collected in 15 ml polypropylene tubes using a fraction collector (LKB-Bromma, Sweden).

The inlet particle solution contained carboxylated polystyrene beads (Bangs Laboratories, Fishers, IN. and Polyscience Inc, Warrington, PA) at a final concentration of 22 mg/L in distilled water. Distilled water containing no microspheres was used for the particle flush. The pH of both solutions was adjusted to pH 7.5. The ionic strength of the particle solution was modified using KBr and KCl to achieve a working concentration of 3.5 mM. The ionic strength of the particle flush solution was modified using KCl exclusively. All solutions were agitated throughout the experiments with samples of the particle and flush solutions taken before and after an experiment to verify constant conditions using flow cytometry.

The basic protocol for all box experiments consisted of:

- Wet packing of the column with glass beads
- Flushing with approximately 5 pore volumes (PV) of the particle-free solution
- 10 PV of particle injection (particles + conservative tracer KBr)
- 10 PV of particle flushing
- Macroscopic real time imaging at set time points throughout experiment
- Microscopic imaging following particle flush
- Image analysis

Excitation of particles was made using a 300W/120V halogen light bulb coupled with an excitation filter corresponding to the particles excitation wavelength. Macroscopic images were captured at set time points using the MagnaFire camera, a cooled CCD digital camera (Optronics) equipped with an emission filter enabling capture of the particles fluorescence. A specially purchased microlens; the VZM 450i from Edmund Industrial Optics, was used for microscopic visualization. Images were analyzed using Image J software (NIH).

MODELING APPROACH

Macroscopic Modeling

To investigate macroscopic particle transport processes, a particle transport model based on the advection-dispersion equation coupled with one-site, two-site and dual-mode kinetic equations was developed. The one-site kinetic model accounts for either a first order irreversible attachment process or a first order attachment-detachment process. The two-site kinetic model has one site for an irreversible attachment process and a second site for the particle attachment-detachment process.

The kinetic model governing equations are:

$$\left\{ \begin{array}{l} \theta \frac{\partial c}{\partial t} + \rho_b \frac{\partial s_r}{\partial t} + \rho_b \frac{\partial s_{ir}}{\partial t} = \theta D \frac{\partial^2 c}{\partial x^2} - v \theta \frac{\partial c}{\partial x} \\ \rho_b \frac{\partial s_{ir}}{\partial t} = k_i \theta c \\ \rho_b \frac{\partial s_r}{\partial t} = k_a \theta c - k_d \rho_b s_r \end{array} \right.$$

where c is the particle concentration in the pore fluid [M/L³], s_{ir} is the irreversible particle concentration associated with solid phase [M/M], s_r is the reversible particle concentration associated with the solid phase [M/M], x is the distance from the particle inlet boundary [L], t is the time [T], D is the hydrodynamic dispersion coefficient [L²/T], v is the average steady state pore fluid velocity [L/T], ρ_b is the bulk density of the solid phase [M/L³], θ is the medium's porosity [-], k_i is the irreversible attachment rate [T⁻¹], k_a is the reversible attachment rate [T⁻¹], and the k_d is the reversible detachment rate [T⁻¹].

To extend to a dual mode kinetic model, the above model was modified to include two additional

parameters: the proportion w [-] and irreversible attachment rate $k_{i,2}$ [T^{-1}] of the second population. The dual-mode mass balance equation is

$$c = (1 - w)c_1 + wc_2$$

where c_1 and c_2 are the first and second particle population concentration in the pore fluid [M/L^3], respectively.

To enable numerical solution of the model equations, a MATLAB program based on a finite difference scheme was developed. The program discretized the time derivative using a Crank-Nicolson approximation, and discretized the space derivative using a central difference approximation. To simulate the column experiments, a Dirichlet boundary condition and Neumann boundary condition were applied at the particle inlet and outlet points of the modeled domain, respectively. The discretized grid size and time step were automatically checked against numerical stability criteria and adjusted accordingly if the criteria were not initially met.

The appropriate kinetic equations for particle attachment and detachment under the experimental conditions were identified through an iterative process of fitting measured data. The estimation of model parameters for each experiment was obtained by minimizing the sum of squared residuals (i.e., the difference between the measured and predicted concentrations) at the four locations of the experimental scan-lines and at the column exit location using the Nelder-Mead simplex algorithm. Residuals were computed in log space for avoiding order related problems.

Microscopic Modeling

To investigate processes influencing microscopic behavior of particles in the vicinity of a rough collector, the Fluent computational fluid dynamics program was used to generate a two-dimensional, steady-state flow field around a nominal, 4mm diameter collection having a sinusoidal perimeter (Figure 3). A grid of over 1,040,000 cells was used in the simulation. Due to limitations in the particle tracking software associated with the Fluent CFD program, a Fortran program was developed to conduct particle tracking within each generated flow field. The program, which includes the effects of Brownian motion, estimates velocity and force vectors normal and tangential to the irregular boundary of the collector as a pre-cursor to forecasting particle attachment at the collector surface. An investigation into the appropriate time step for

simulations revealed that a time step of 10PRT, where PRT is the particle relaxation time, produced the most consistent results. At lower relaxation times, particles tended to stagnate during transport while higher relaxation times produced unstable results and predicted particle displacement modes that opposed local velocity fields.

Modeling of particle tracking was conducted for particles with diameters of 2- μm , 7- μm , 15- μm and 25- μm , respectively for the parameters shown in Table 1. The specific gravity of the particles was assumed to be 1.1 or 1.5. Free flow fields were downward, upward or at 45 degrees to the collector. For each simulation, there was a possibility of 6088 entry points to the capture zone around the collector. One particle was released at each entry point, and then tracked to determine its trajectory over time.

ACCOMPLISHMENTS

Column experiments

The results of the column experiments are summarized in Table 1, listed as experiments C1 to C4. Duplicate particle breakthrough curves for the upward, downward and horizontal flow of 1- μm particles are shown in Figure 4. Minimal variation is shown in duplicate columns for each flow direction. Differences in the irreversible attachment rates (k_i) was observed for upward ($k_i = 5.49 \times 10^{-5} \text{ s}^{-1}$ for C2), downward ($3.78 \times 10^{-5} \text{ s}^{-1}$ for C3) and horizontal ($6 \times 10^{-5} \text{ s}^{-1}$ for C1) flow). The spatial distribution of microspheres is shown following the termination of the column experiments (Figure 5). Maximum attachment of microspheres was evident within the first 1.5 cm following entry into the column, irrespective of flow direction. The retained profiles for upward flow followed classic filtration theory (log-linear decrease). However, the retained profiles for both downward and horizontal flow deviates from classic filtration theory with an initial decrease in particle retention, followed by an increase half way through the column (6-7.5cm).

Increasing ionic strength from 3.5 mM to 20 mM increased the retention of particles within the column ($k_i = 4.25 \times 10^{-4} \text{ s}^{-1}$ (Table 1 Experiment C4)). The maximum attachment of microspheres was again evident within the first 1.5 cm following entry into the column with profiles following the same trend observed after upward flow under less favorable conditions (Figure 5).

Rectangular box experiments

After initial problems in relation to low particle fluorescence and imaging (MagnaFire software compatibility) a method was developed that enabled the real-time spatial resolution of micron-sized particles. Differentiation between the co-transport of 1-um (envy green) and 6-um (yellow green) particles was also possible with the use of 530/590 nm and 450/530 nm filter pairs, respectively (Figure 6).

The real-time spatial resolution of particles was accomplished by illuminating and photographing the entire flow field of the box at set time points. Due to light scattering the fluorescent light intensity at one location is not only determined by its concentration but also by its surroundings. Therefore, a band filter consisting of seven discrete scan lines was placed over the front of the box (Figure 7). These scan lines are 1 cm high by 3 cm long, and 1 cm apart from each other in depth. Scan lines 1 and 7 allow measurement of inlet and outlet (BTC) zones. Scan lines 2 to 6 allow measurement of the collector matrix filled area. Individual calibration curves were used for each scan line. The fluorescence intensity of all particles was stable with little variation due to illumination time. Figure 8 provides an example of this stability for 1-um particles.

The real-time spatial resolution of 1- μ m particles (Table 1, A3), 3- μ m (Table 1, A4), 6- μ m (Table 1, A5), 1-25- μ m mixed particles (Table 1, J1 to J3), as well as 1- μ m with 6- μ m particles present (Table 1, A7), and 6- μ m with 1- μ m particles (Table 1, A6) present were determined under downward flow through an acrylic box packed with 0.5 mm diameter glass beads. Irreversible attachment rates were obtained from the normalized plateau concentration of the BTC. In all cases the concentration of particles within the output (plateau concentration) was lower than the input concentration irrespective of particle size. This indicates that a fraction of the particles were filtered out by the porous medium. Table 1 provides a summary of the experimental conditions and irreversible attachment rates obtained from the particle BTCs. Results indicated:

- Breakthrough plateaus decreased when particle size increased.
- Large difference in irreversible attachment rates observed between 1- μ m and $\geq 3\mu$ m particles.
 - 1- μ m downward flow (average $k_i = 6.15 \times 10^{-5} \text{ s}^{-1}$)
 - 3- μ m downward flow ($1.03 \times 10^{-4} \text{ s}^{-1}$)

- 6- μm downward flow (average $k_i = 1.11 \times 10^{-3} \text{ s}^{-1}$)
- Difference in irreversible attachment rates for the upward and downward flow of mixed 1-25- μm particles was minimal
 - Upward flow ($0.92 \times 10^{-3} \text{ s}^{-1}$)
 - Downward flow ($1.00 \times 10^{-3} \text{ s}^{-1}$)
- Competition between particles for attachment sites was observed when two different sized particles were present.
- Breakthrough plateaus were lower when 1- μm or 6- μm particles were used exclusively (Figures 9)
 - Irreversible attachment rates for 1- μm particles decreased when 6- μm particles were present ($k_i = 6.15 \times 10^{-5} \text{ s}^{-1}$ / 1.19×10^{-5} to $k_i = 7.34 \times 10^{-6} \text{ s}^{-1}$)
 - Irreversible attachment rate decreased for 6- μm particles when 1- μm particles were present ($7.97 \times 10^{-4} \text{ s}^{-1}$ / 1.11×10^{-3} to $1.13 \times 10^{-4} \text{ s}^{-1}$)

The retained profiles at various depths and their corresponding images for particle experiments are shown in Figure 10. In general, the bulk of particle retention took place within the first 1 cm of the column (Figure 10). However, the retention of 1- μm particles was more homogeneous throughout the entire column when compared to the larger particles used. The retention of 6- μm particles was reduced in the first 1 cm when 1- μm and 6- μm particles were run together. The opposite was true for 1- μm particles, which, in the presence of 6- μm , particles were increasingly retained within the first 3 cm – this is possibly attributed to pore space blockage. The retained 6- μm particles were also transported deeper into the matrix (3 cm) when 1- μm particles were present. The real-time spatial resolution of 1- μm and 6- μm particles, both exclusively and combined, are shown in Figures 11 and 12. For 1- μm particles (Figure 11), real-time spatial resolution profiles indicate that particles are evenly distributed throughout the entire box (Exp A3.1). In the presence of 6- μm particles, the retained 1- μm particles were transported deeper (3 cm) (Figure 11). For 6- μm particles, the interior particle concentration exhibited similar trends irrespective of whether 1- μm particles were present (Figure 12). In all cases, during the particle injection phase a nonlinear increase in the concentration of 6- μm particles was observed with time, prior to a linear increase once the pore fluid concentration reached steady state. When particle injection was stopped after 10PV, any 6- μm particles reversibly attached to the collector

matrix were remobilized and flushed out of the box. The concentration of reversibly attached 6- μm particles was higher in the presence of 1- μm particles. The real-time spatial resolution for 3- μm particles followed a similar trend to that exhibited by 6- μm particles when used exclusively (Figure 14). The BTC for 3- μm particles is shown in figure 13.

Following the particle flushing (10PV), microscopic images at various depths throughout the box were taken. Images for 6- μm particles with and without 1- μm particles reveal that interaction between 6- μm particles and the collector occurred primarily at the top surface and at the contact points between collectors. (Figure 15)

Macroscopic Modeling Results

Additional experiments were conducted in the rectangular column set-up to generate further data for the macroscopic modeling work (Table 1, D1 to H4). Table 2 provides the parameter estimation summary of the macroscopic modeling results for 1- μm , 3- μm and 6 μm particles with downward flow conditions. Figures 16-19, 20-23, and 24-27 compare modeling and experimental results for a one-site irreversible model ($s_r = 0$), a one-site reversible model ($s_i = 0$), a two-site model including irreversible and reversible attachment, and a dual mode model with two particle populations, for the 1- μm , 3- μm , and 6- μm particles, respectively. Figures 28-31 and 32-35 present results from mixed 1 μm and 6 μm simulations, respectively.

Figures 16, 20, and 24 present the 1-site irreversible modeling results. As with the results presented in Table 1, the larger size particle has the higher estimated irreversible attachment rate, consistent with the fact that particle retention decreases with decreasing particle size (see Table 2). Fitting of both the scan line data and the BTC data reduces the estimated k_i values reported in Table 1, demonstrating that particle transport parameters obtained from BTC data alone might not fully capture particle fate and transport. As seen in Figures 16, 20, and 24 the irreversible model does fit peak concentrations well for 1- μm and 3- μm particle cases, but not fit well the entire range of observed behavior, nor data from the 6- μm particle test.

For the reversible model, as shown in Figure 17, 21 and 25, 1- μm and 3- μm particle attachment rates are similar and the estimated 6- μm particle attachment rate is larger, however, the 1- μm

particle has the highest detachment rate as the retained particle concentration was lower. The ratio of attachment and detachment rates controls the shape of the rising limb and tail of the breakthrough curve and all scan-lines. Compared with the irreversible model, a better fit to experimental data is obtained, and the Residuals are all decreased from double digits to a single digit. Although the residual of 6-um test is also reduced, the modeling results are still not a good fit with the observed data.

For the 2-site model (Figures 18, 22 and 26), the 1-um particle population has the lowest irreversible attachment of all three particle sizes due to the low retained particle concentration of all scan-lines. The estimated small irreversible rate indicates that the 1-um particle behavior might conform to a reversible model assumption. Similar to reversible model, the 2-site model also overestimates observed peak concentrations. For the 3-um particles, all attachment and detachment rates are comparable. The 2-site model has a slightly smaller residual than the 1-site reversible attachment model for the 3-um particles. Comparing figure 21 with figure 22, the 2-site model improves the rising limb and tails of all scan-lines and the breakthrough curve, especially during the transition time (around 10 pore volumes). However, the 2-site model had the same issue as the 1-site reversible model in fitting of the final retained particle concentration. For the 6-um test, the 2-site model does not perform well and has higher residual than reversible model, because the 2-site model overestimates all scan-line peak concentrations simultaneously. Figures 24-26 shows that single population models are not capable of describing 6-um particle transport activities in column (scan-lines) and effluent (breakthrough) concentrations.

For the dual mode model (Figures 19, 23 and 27), all particle sizes have a small fraction of the population with a fast irreversible deposition rate, with the fraction increasing with particle size and the irreversible rate decreasing with particle size. In all cases, residuals for this model are the lowest of all of the four models, leading to the conclusion that the dual model better captures particle behavior than the other models. Of note is the fact that the dual model is the only model that can fit the observed 6-um particle behavior.

Experiments and modeling results for 1-um with 6-um particles present, and 6-um with 1-um particles present, are provided in figures 28-31, and 32-35, respectively. For 1-um with 6-um

particles present, the experimental results are similar to those from the pure 1-um tests. All scan-lines have low absorbed concentrations, and the breakthrough plateau is close to $C/C_0 = 1$. For this condition, the irreversible model has largest residual because the irreversible model cannot fit the lag time of the scan-lines and breakthrough curve. The reversible model reduces the residual to 1.03. Comparing figures 29 and 30, the reversible model overestimates the plateau concentration but fits the rising and decreasing concentrations better. The 2-site model converges to the reversible model with a small irreversible attachment rate, which results in higher predicted retained concentrations for each of the scan-lines. In contrast, the dual mode model converges to the irreversible model. For 6-um with 1-um particles present, only the dual mode model can catch the peak concentration and rising/decreasing limbs simultaneously. Comparing tests with 6-um only and 6-um with 1-um present, the mixed test has a slightly higher population with a larger irreversible attachment rate, and the 2nd population has a lower reversible attachment and detachment rate. Thus, the fitting results indicate the presence of the 1-um particles enhances 6-um particle deposition. This is consistent with the experimental results, which show that the mixed particle test has higher retained concentrations for all scan-lines.

Modeling results of 1-um and 6-um particle transport under upward and horizontal flow condition are still in progress. Initial experimental results and irreversible modeling results are presented in figures 36-39. For both 1-um and 6-um particles, the peak concentrations decreased from upward to horizontal to downward flow conditions. The phenomena that is most different between test data is the rising limb of the breakthrough curve. The rising limb changes from steep increasing to mildly increasing as the flow direction changes from downward to upward. The horizontal flow conditions appear to cause more complex transport phenomena because of the perpendicular effects of body force. Specifically, the horizontal breakthrough curve shows a non-smooth rising limb which is different than seen in the other two cases. The difference between scan-line peak concentrations indicate that more particles are attached under upward and horizontal flow conditions, than downward flow conditions. These results are all consist with the hypothesis that flow direction does have a significant influence on particle fate and transport in porous media.

S. K. Ngueleu, P. Grathwohl, and O. A. Cirpka (2013), Effect of natural particles on the transport of lindane in saturated porous medial: Laboratory experiments and model-based analysis, JCH:13-26

Particle Tracking Results

The system parameters used in the particle tracking analyses are shown in Table 3, while Table 4 gives a summary of the variables that were investigated. A negative velocity in the y-direction with zero velocity in the x-direction is downward flow, whereas a positive velocity in the x-direction with zero velocity in the y-direction is horizontal flow. Figure 40 provides an example of trajectories followed by the particles for a case where flow is 45 degrees to the horizontal. As seen, the particles either attached to the collector, or exited the unit cell.

The collector efficiency, η , is defined as the ratio of the number of particles attached to the collector surface to the total number of particles entering the cell. Collector efficiencies for four different particle sizes at an approach velocity of $-5.49 \cdot 10^{-4}$ m/sec in the -y-direction (downward flow) are shown in Table 5. The collector efficiency is relatively low for the particles of $2 \cdot 10^{-6}$ m diameter. As the particle diameter increases, the collector efficiency also increases. More than half of the particles having a diameter of $7 \cdot 10^{-6}$ m or greater, attached to the collector surface. For the particles of $25 \cdot 10^{-6}$ m diameter, the attachment rate is 64.3 per cent, which is the highest efficiency obtained in the numerical simulations that were conducted occurring for particles having specific gravity of 1.1. The results are in good agreement with those obtained by previous models and experiments, revealing that simulated collector efficiencies show a minimum value for particle sizes ranging from $1 \cdot 10^{-6}$ to $3 \cdot 10^{-6}$ and increase with particle diameter.

Simulations were carried out using the an approach velocity of $-5.49 \cdot 10^{-4}$ m/sec in -y-direction in order to evaluate the effect of particle specific gravity on collector efficiency, Table 6. Particles of $25 \cdot 10^{-6}$ m diameter having a specific gravity 1.5 attached to the collector at the rate of 81.1 per cent, which is significantly higher than the attachment rate of the relatively lighter particles of the same size. Therefore, it can be concluded that the specific gravity of particles has a dominant effect on collector efficiency for the conditions of the numerical simulations.

For three different approach velocities in the -y-direction, the collector efficiency decreased with a decrease in the fluid velocity. The fast vertically downward approach velocity of $5.49 \cdot 10^{-4}$ m/sec yielded the highest efficiency of 55.6 per cent as shown in Table 7. When the approach

velocity is halved, as in the case of medium vertically downward approach velocity of $2.76 \cdot 10^{-4}$ m/sec, the efficiency decreased to 53.5 per cent. For the slow approach velocity of $1.38 \cdot 10^{-4}$ m/sec, the collector efficiency further dropped to 43.7 per cent. Such a trend is in agreement with the trends reported in previous models and experiments, asserting that the simulated collector efficiency for a given particle size scales up with increasing velocity.

Work is on-going analyzing the spatial distribution of attached particles on the collector for the three different flow conditions investigated. Initial results indicate that the number of particles accumulated on the ridges of the collector surface is much higher than that of the particles stuck to caves on the collector surface. The gravity and the flow direction were the principal determinants of the locations where the particles attached to the collector surface or exited the cell. In the cases of downward and horizontal flow, particle clusters were formed on the sides of the ridges. However, in the case where the approach velocity was at an angle of -45° to the x -axis, the particles only accumulated on the side of the ridges that faced the flow direction. For all three flow directions, most particles exited the cell above the caves of the collector.

SUMMARY

Overall, the research project collected data from about 40 experiments and undertook both macroscopic and microscopic modeling of particle fate and transport under numerous different conditions. The results of the work clearly demonstrate the influence of particle size, specific gravity and flow direction on particle transport mechanisms. The work has also highlighted that the location of particle attachment sites on a collector surface is dependent on flow direction. Current models for particle fate and transport do not account for the complexity of transport phenomena uncovered by this research. As a result, predicting particle fate and transport under field, or even controlled laboratory, conditions remains challenging.

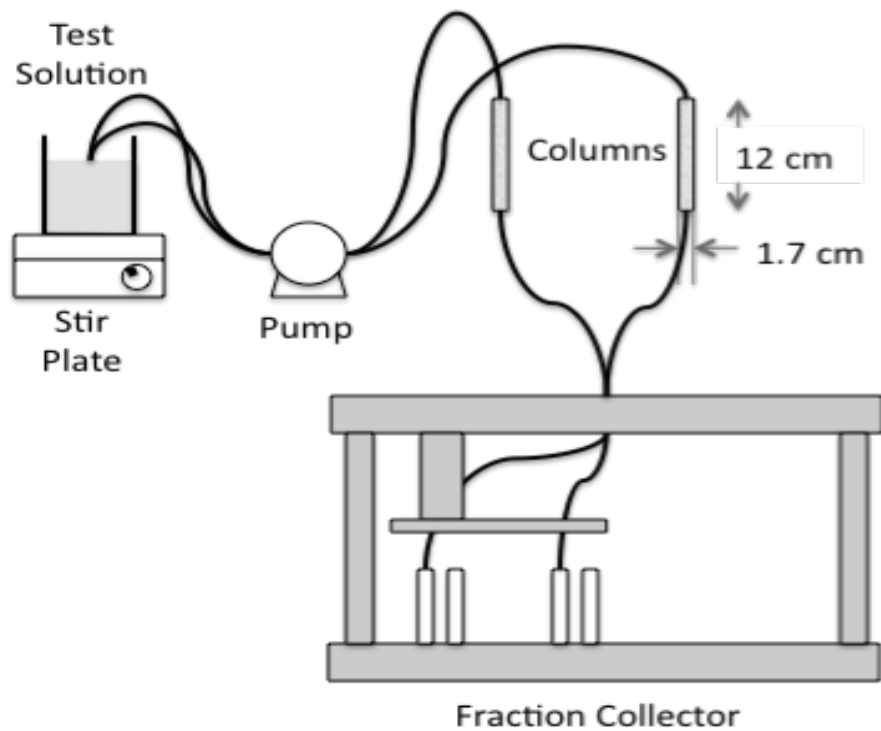


Figure 1. Experimental set-up for column experiments

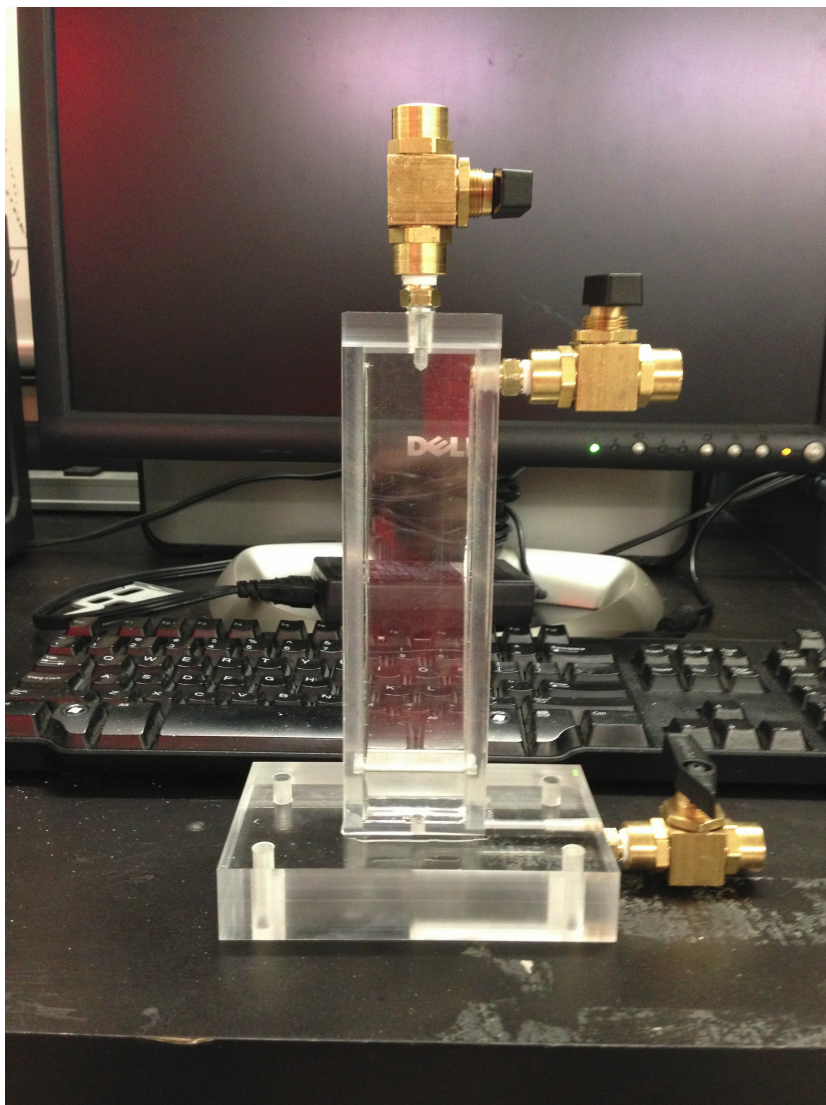


Figure 2. Photograph of equipment used in rectangular box experiments

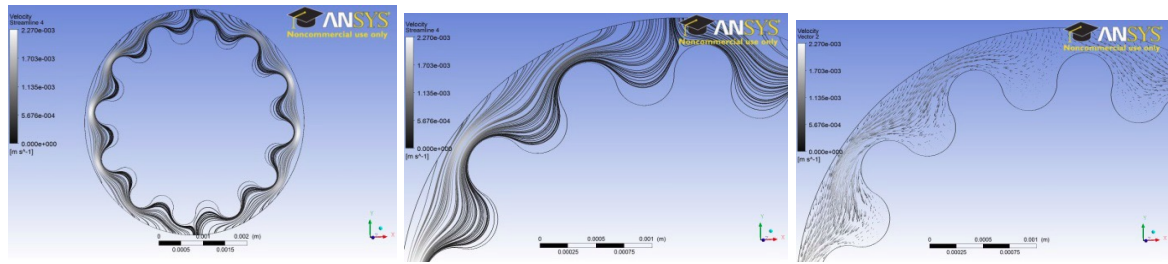


Figure 3. Streamlines and velocity vectors around the collector for the slow vertically downward approach velocity ($v_x = 0$ and $v_y = -1.38 \cdot 10^{-5}$ m/sec)

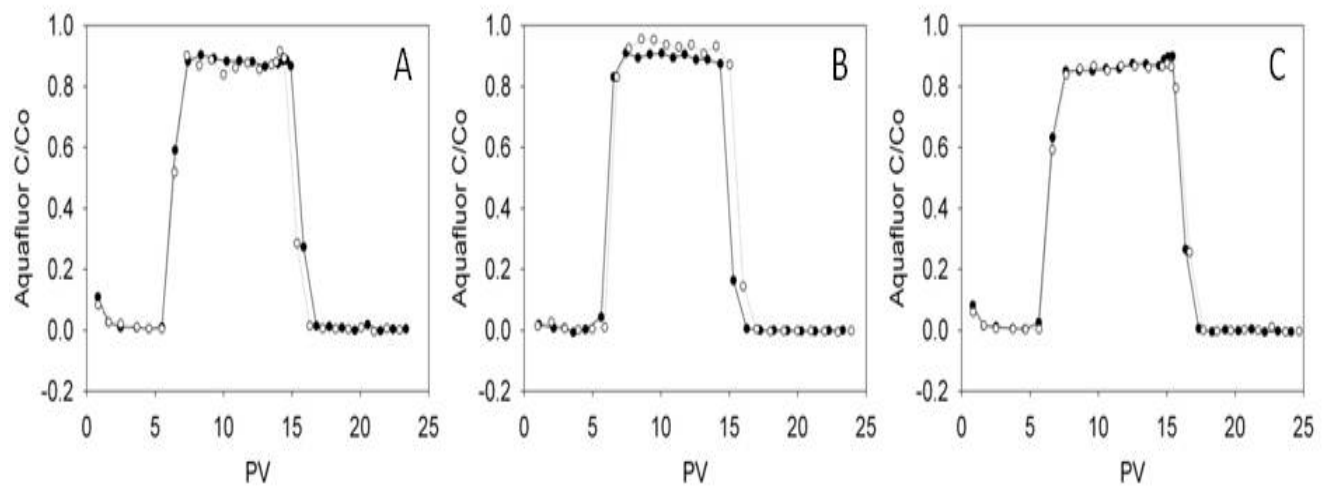


Figure 4. Duplicate breakthrough curves for the 1- μm particle transport tests under upward (A), downward (B) and horizontal (C) flow conditions. Particle solutions consisted of 0.5 mg/L particles at pH 7.5 and 3.5mM ionic strength. Breakthrough concentrations are normalized by the inlet concentration.

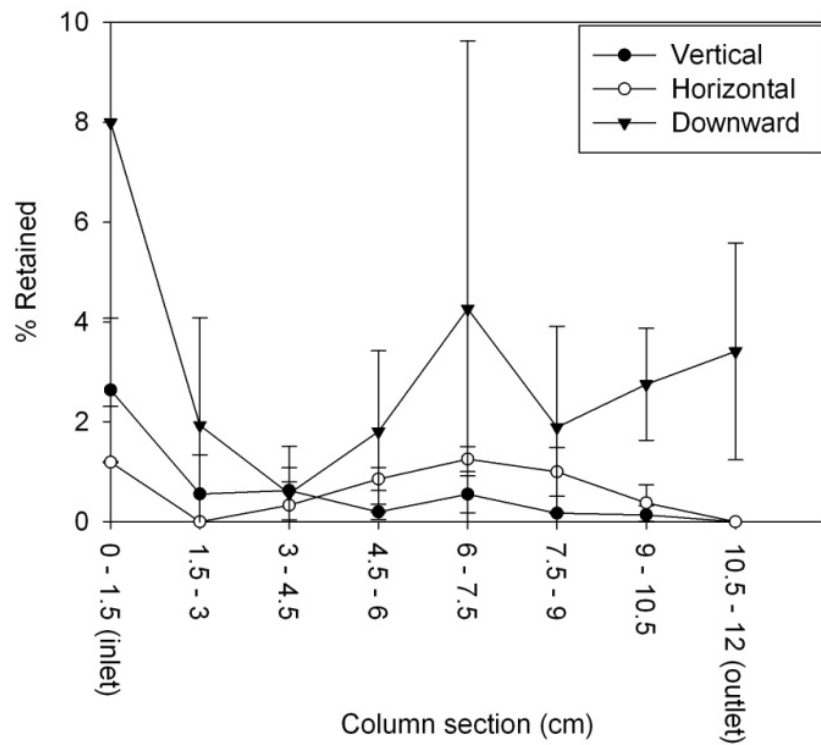
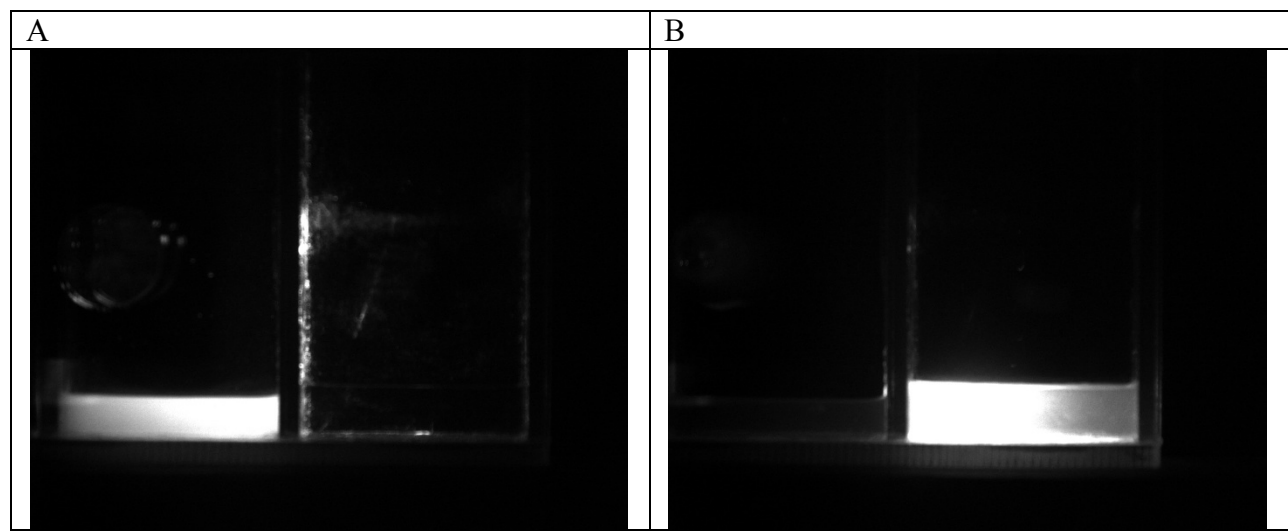


Figure 5. Retained profiles for columns following upward, downward and horizontal flow of 1- μm microspheres. Error bars represent standard deviations from replicate experiments (n=2).



1-um

6-um

1-um

6-um

Figure 6. Differentiation of 1-um and 6-um particles using (a) 530/590 nm and (b) 450/530 nm filter pairs



Figure 7. Band filter with scan lines

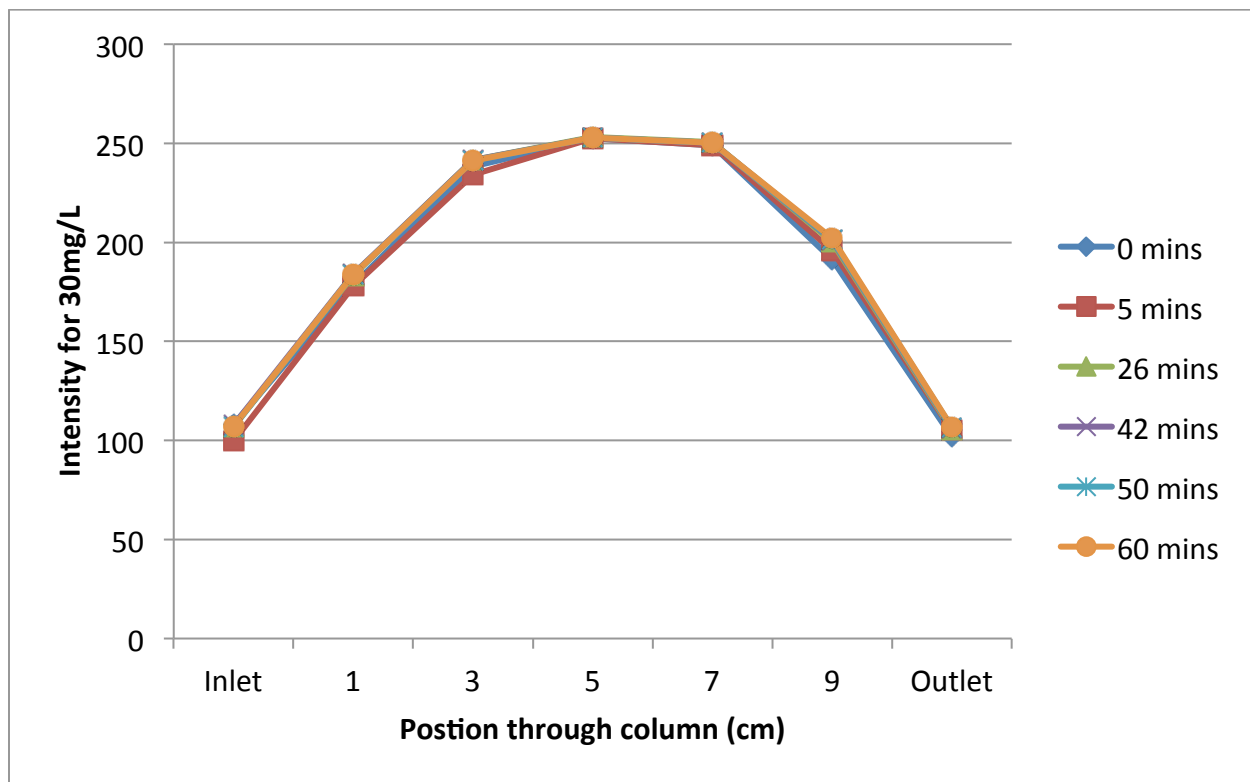
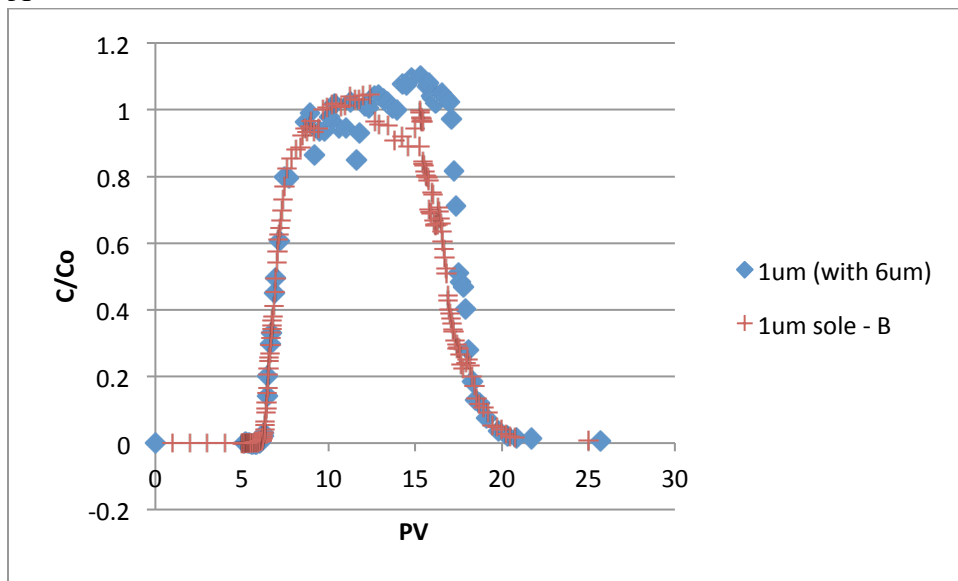


Figure 8. Influence of illumination time on particle fluorescence intensity

A



B

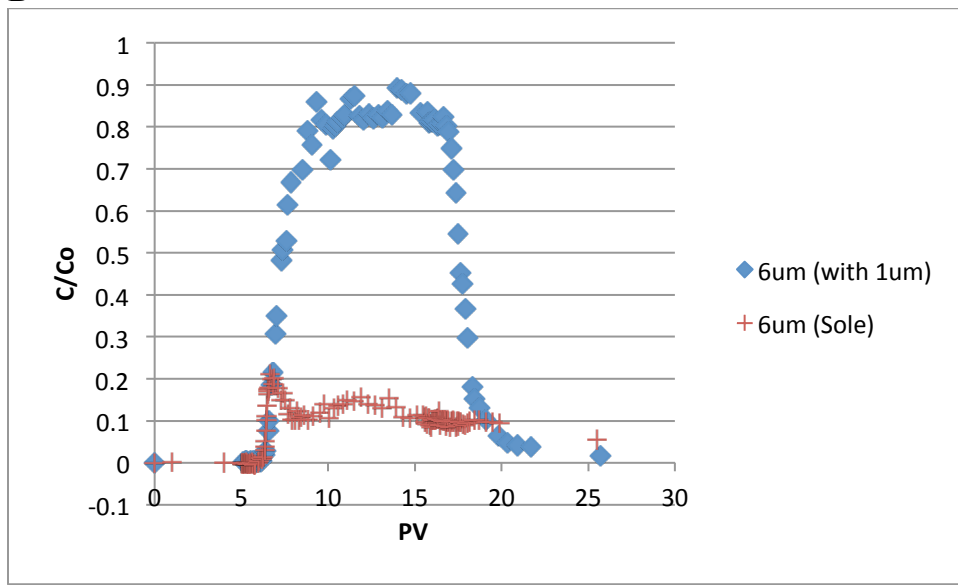


Figure 9. Breakthrough curves for downward flow of 1-um particles with (exp: A7) and without (exp: A3.2) 6-um particles. 6-um particles with (exp: A6) and without (exp: A5.2) 1-um particles (b). Conditions are listed in Table 1.

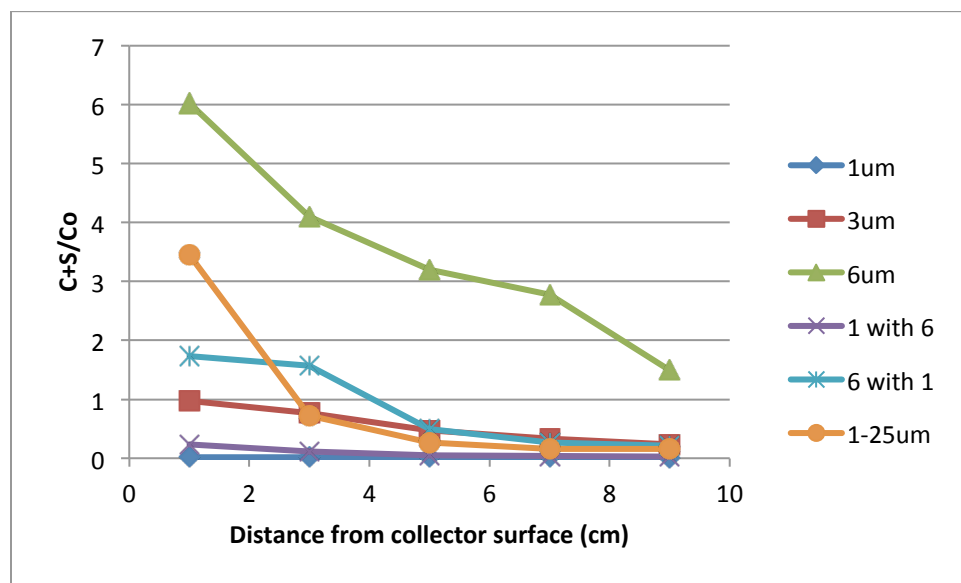
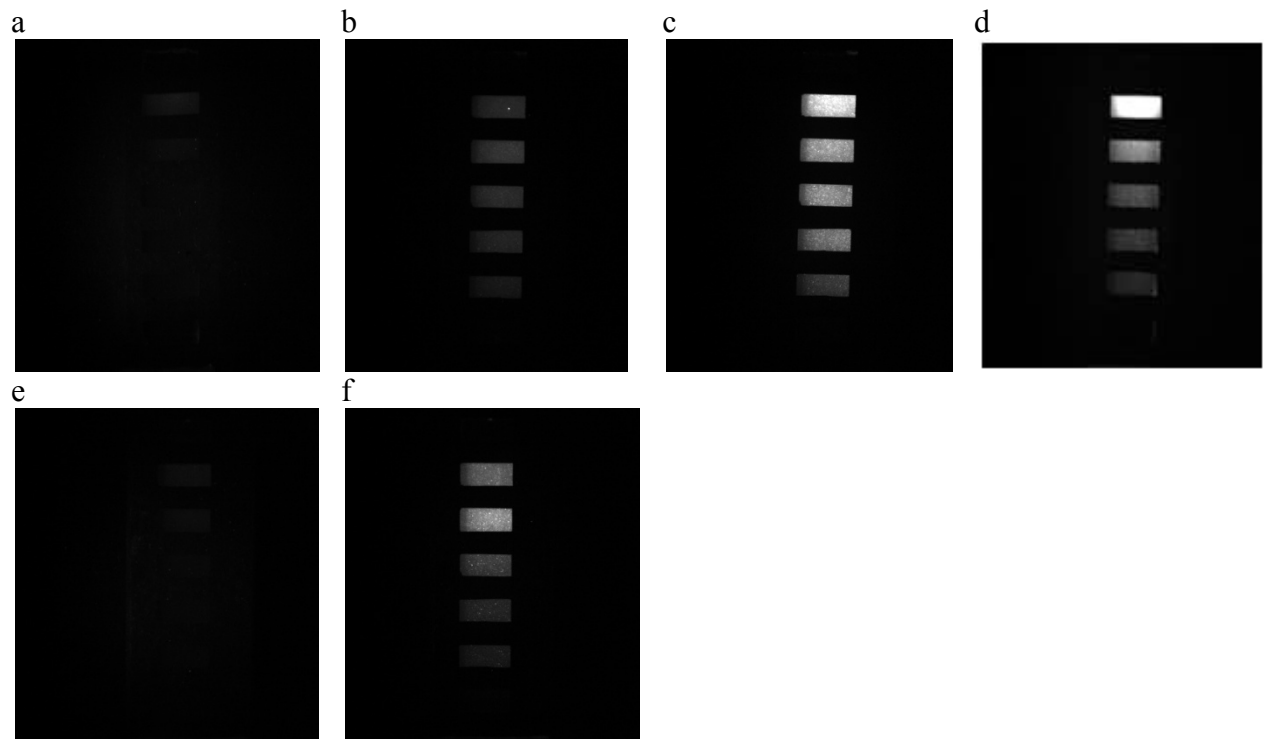


Figure 10. Scan line images and retained profile following a 10PV flush for (a) 1-um particles (exp A3.2), (b) 3-um, (c) 6-um particles, (d) 1-25-um, (e) 1-um with 6um particles present, and (f) 6-um with 1-um particles present.

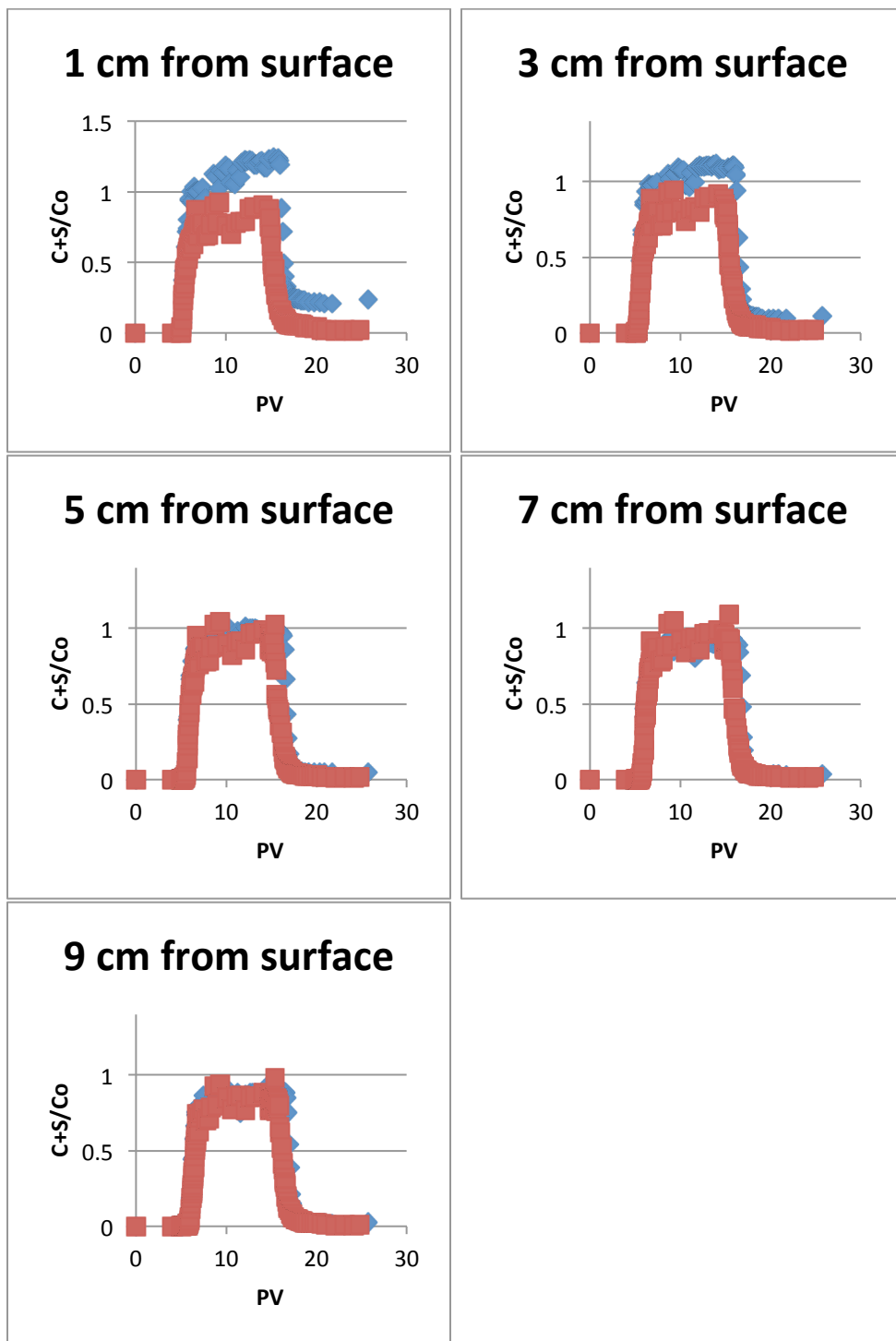


Figure 11. Interior concentration with time for 1-um particles exclusively (red EXP A3.1) and when 6-um particles are present (blue): (a) 1 cm below the inlet surface, (b) 3 cm, (c) 5 cm, (d) 7 cm, and (e) 9cm. Experiment A3.1 and A6.

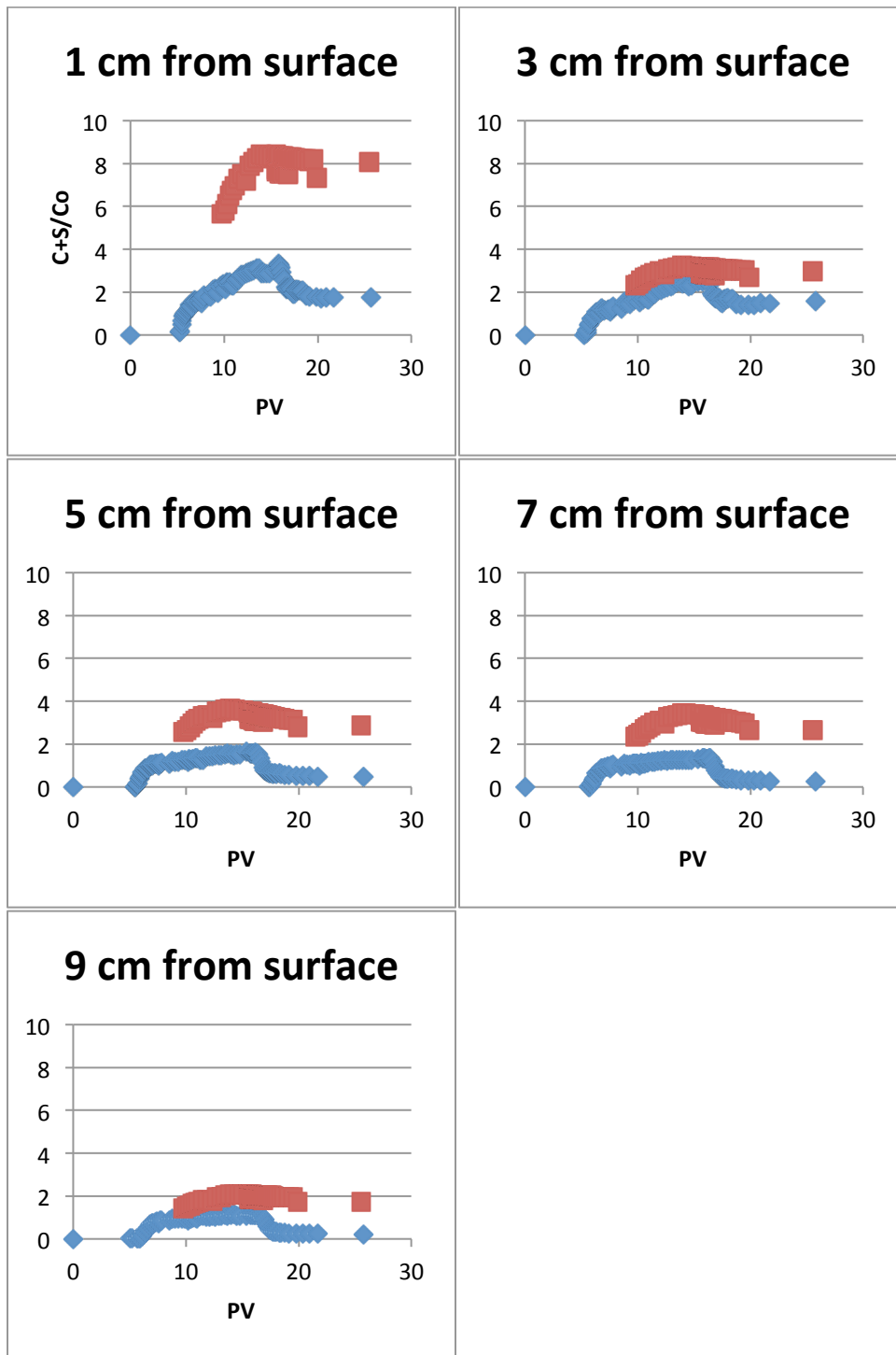


Figure 12. Interior concentration with time for 6-um particles exclusively (red) and when 1-um particles are present (blue): (a) 1 cm below the inlet surface, (b) 3 cm, (c) 5 cm, (d) 7 cm, and (e) 9cm. Experiment A5.1 and A6.

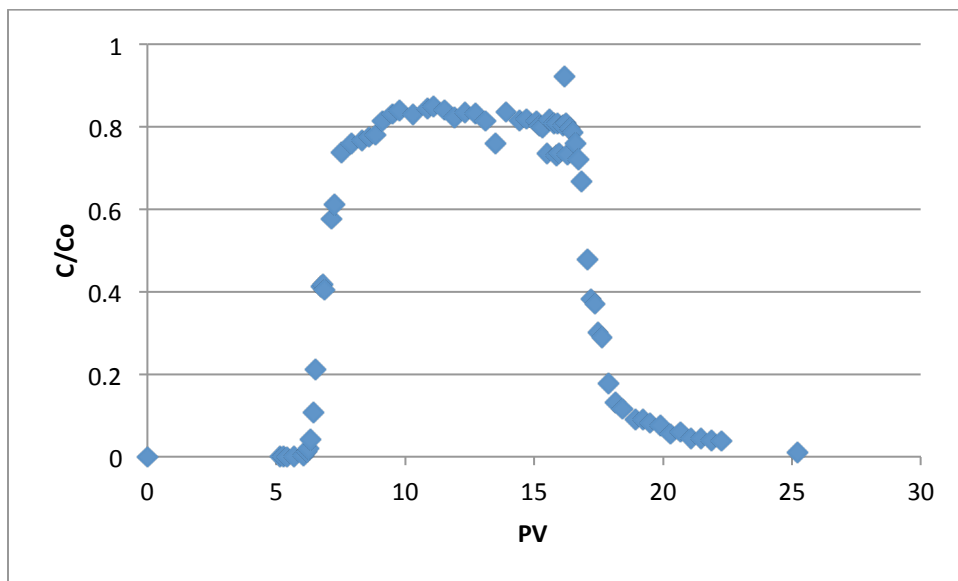


Figure 13. Breakthrough curves for downward flow of 3-um particles. Experiment A4.

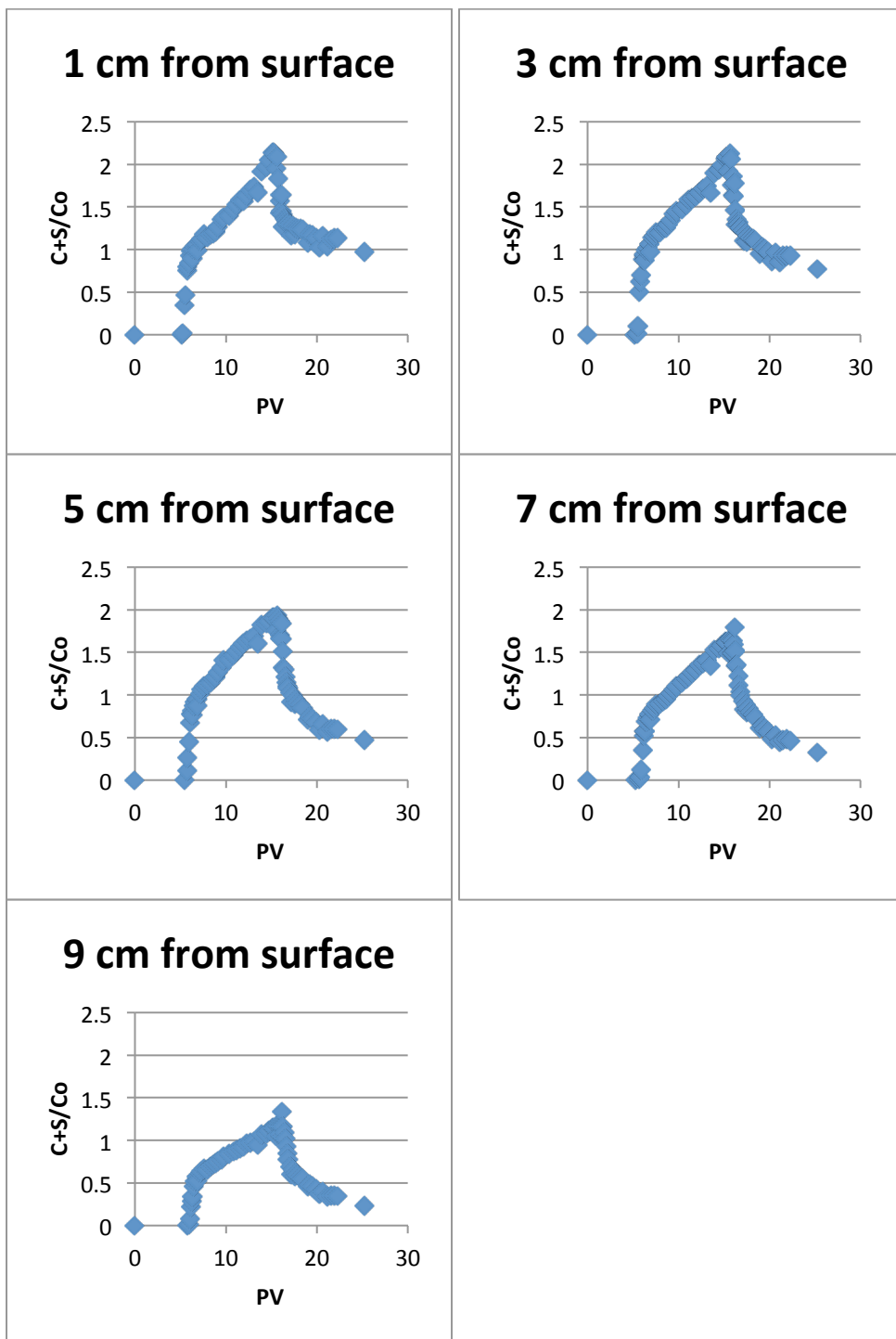


Figure 14. Interior concentrations with time for 3-um particles: (a) 1 cm below the inlet surface, (b) 3 cm, (c) 5 cm, (d) 7 cm, and (e) 9cm. Experimental details are shown for A4.

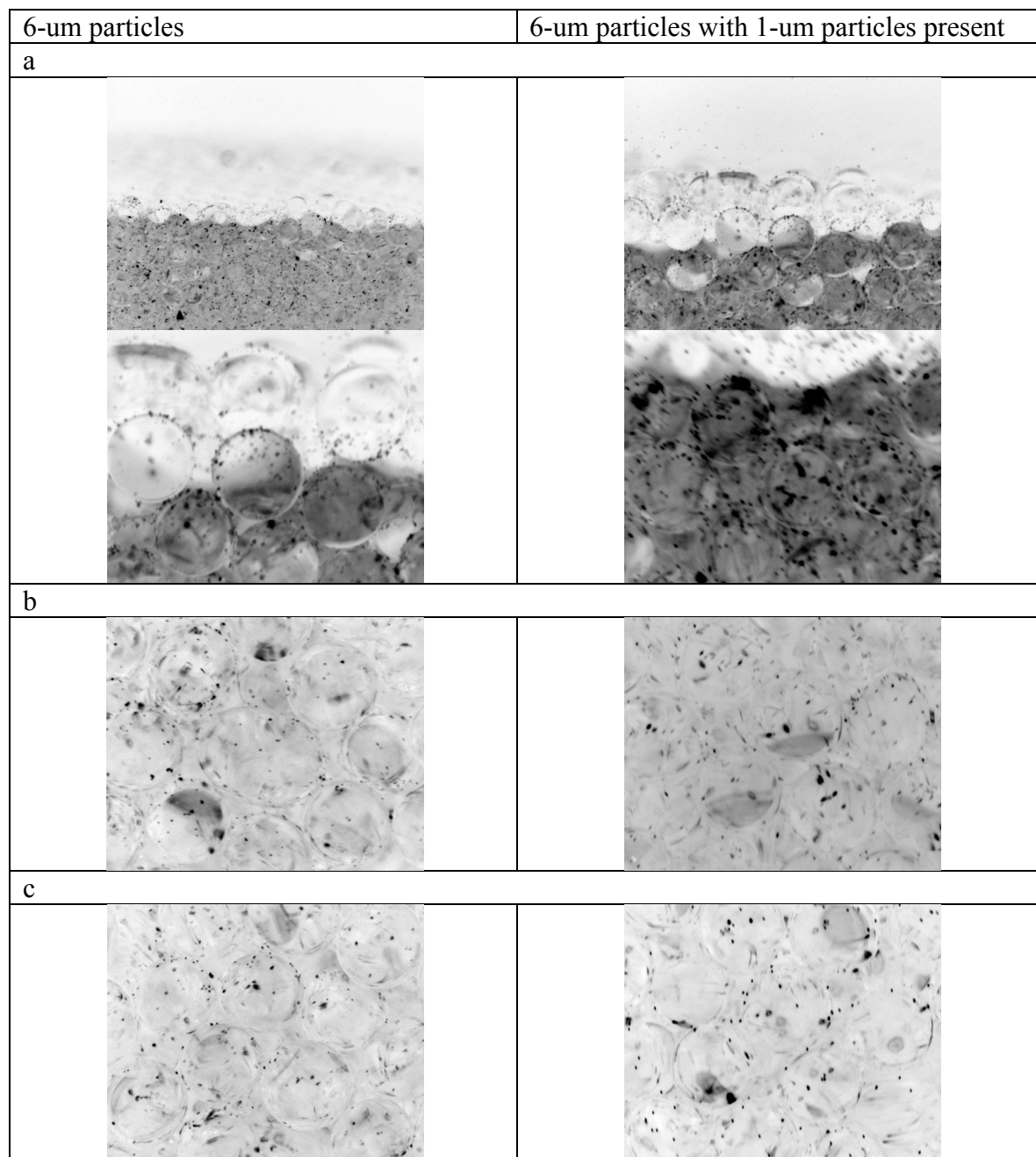


Figure 15. Microscopic observations of retained 6-um particles exclusively and when 1-um particles were present following 10PV flush. (a) Inlet surface, (b) 3 cm below inlet surface, and (c) 5 cm.

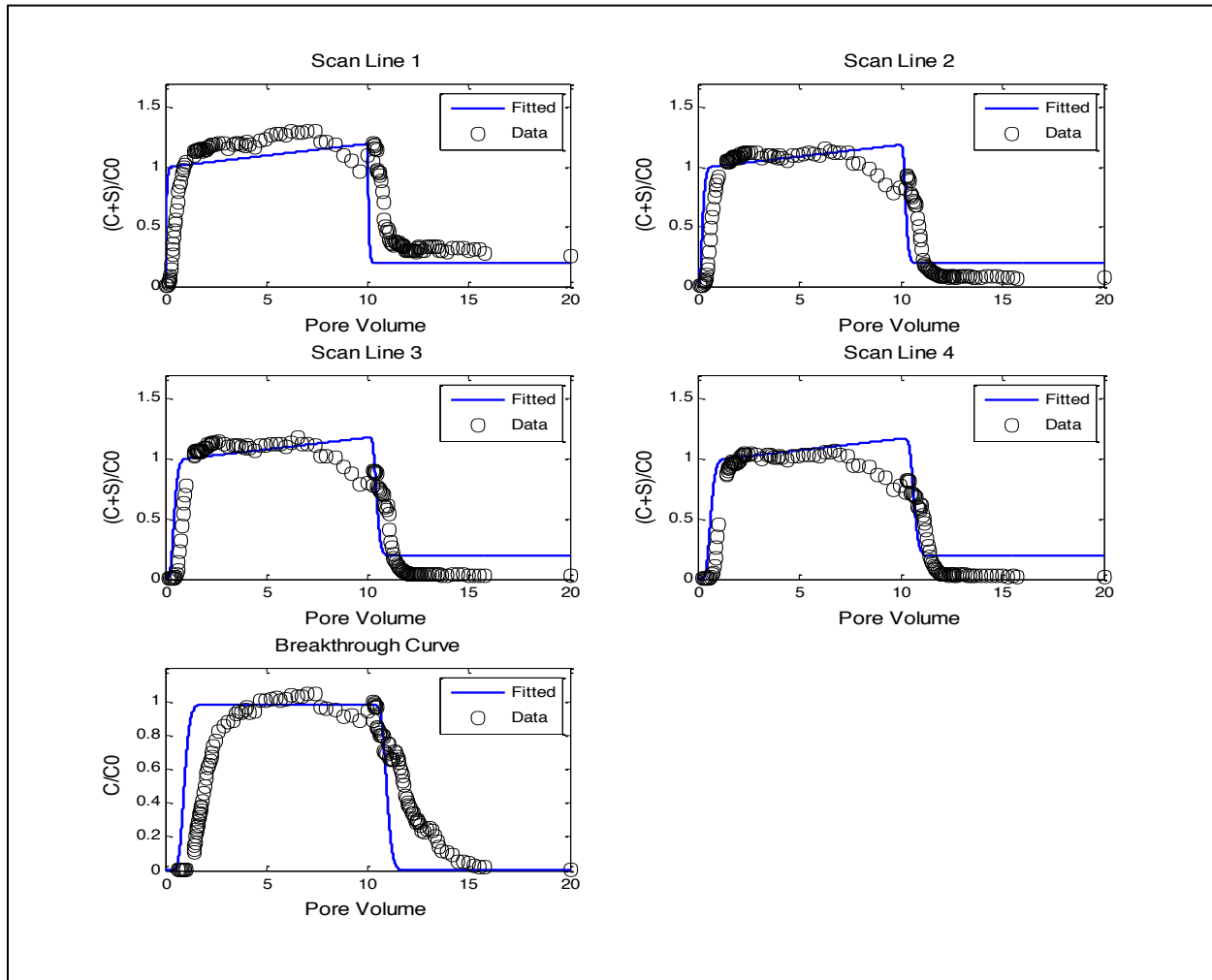


Figure 16. Simulated 1-um particle transport via 1-site irreversible attachment model. Comparison shows that the irreversible model can fit measured data with respect to peak concentration. However, the model does not capture the overall shape of the particle concentration curves.

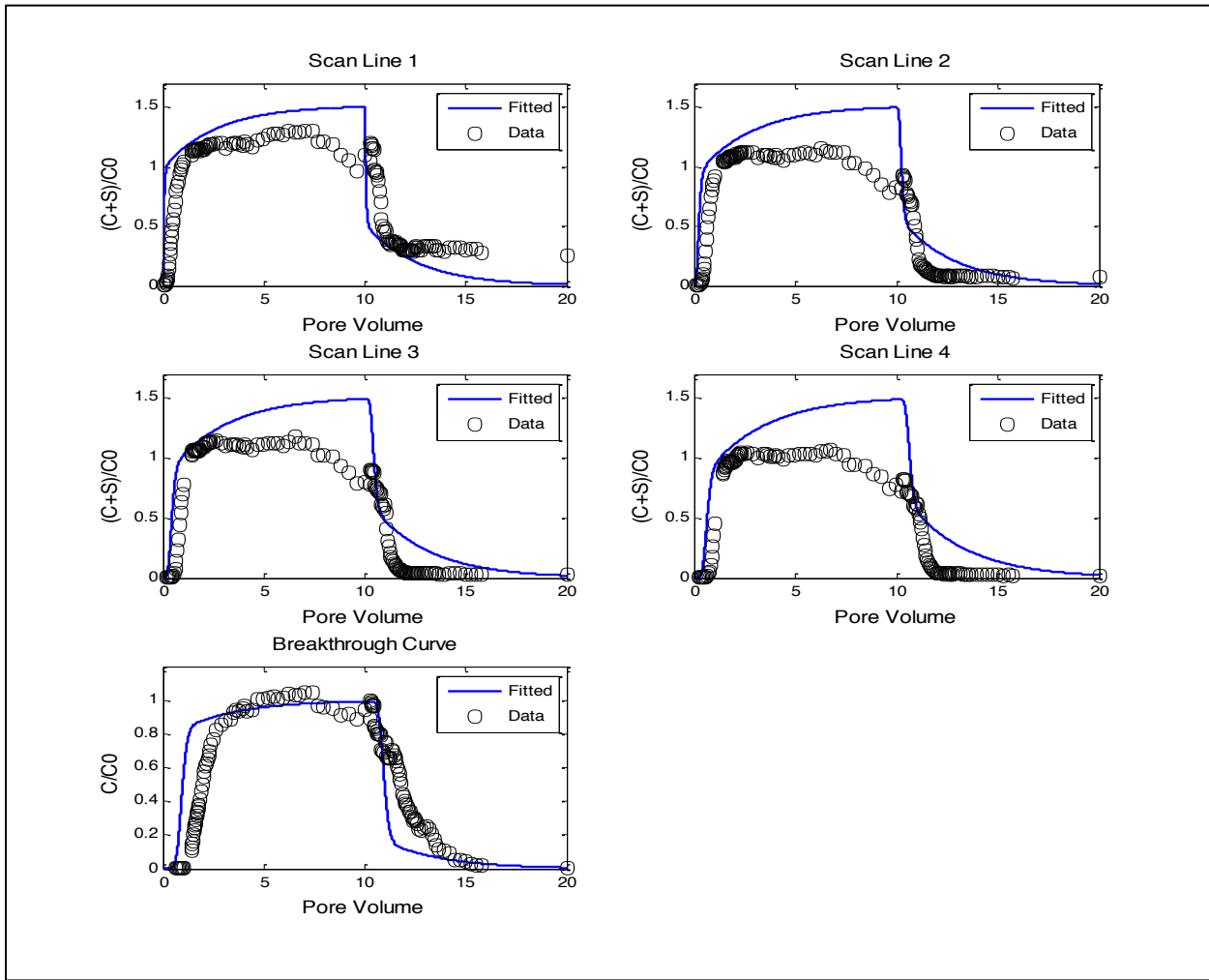


Figure 17. Simulated 1-um particle transport via 1-site reversible attachment and detachment model. Results showed that the reversible model fits the breakthrough curve well. However, the reversible model overestimated all scan-lines' peak concentration and poorly fitted all scan-lines' tails.

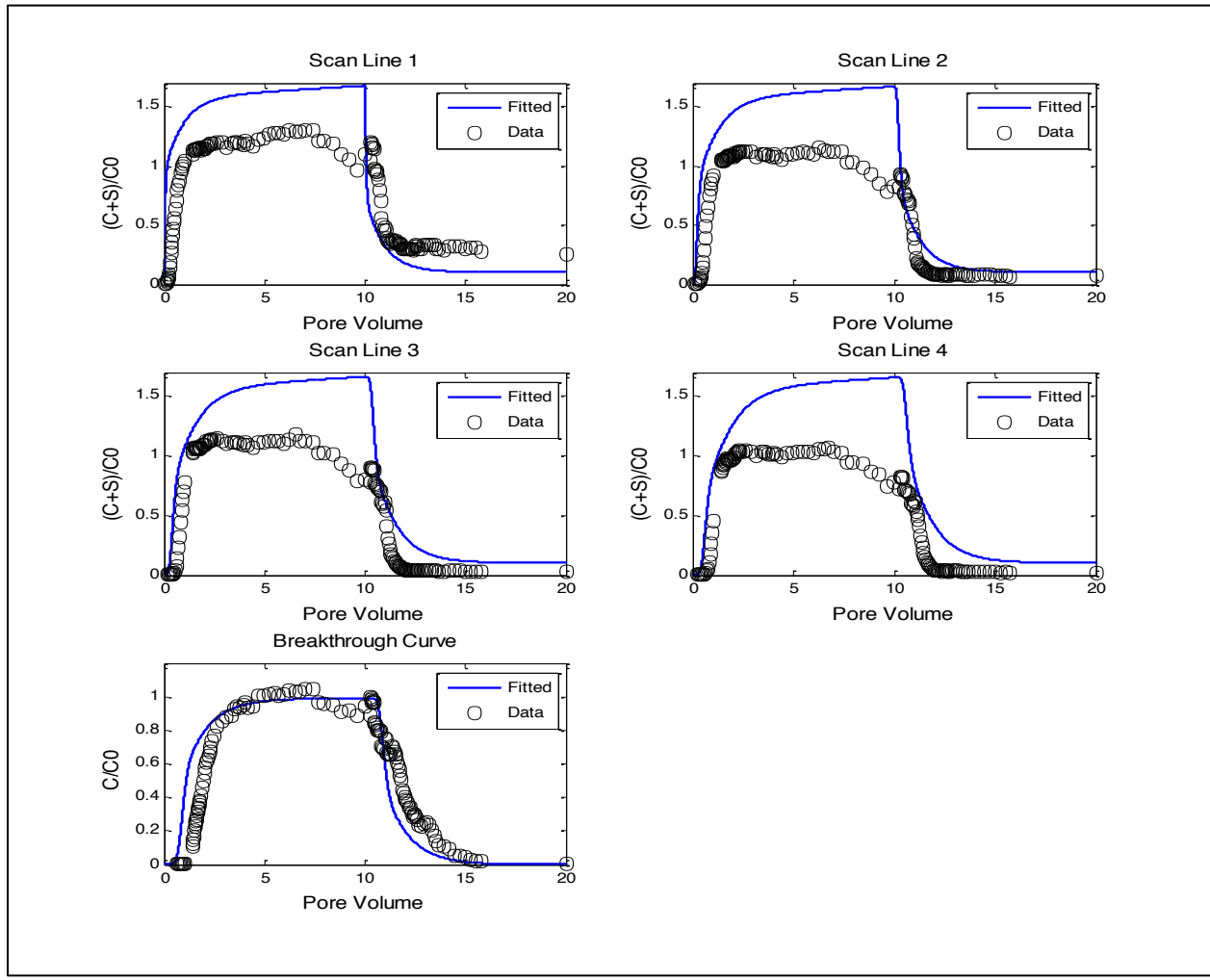


Figure 18. Simulated 1-um particle transport via 2-site kinetic model. Results show that the 2-site model fitted the measured breakthrough curve and all scan-line tails better than the 1-site models. However, there was overestimation of all of the scan-lines' peak concentration.

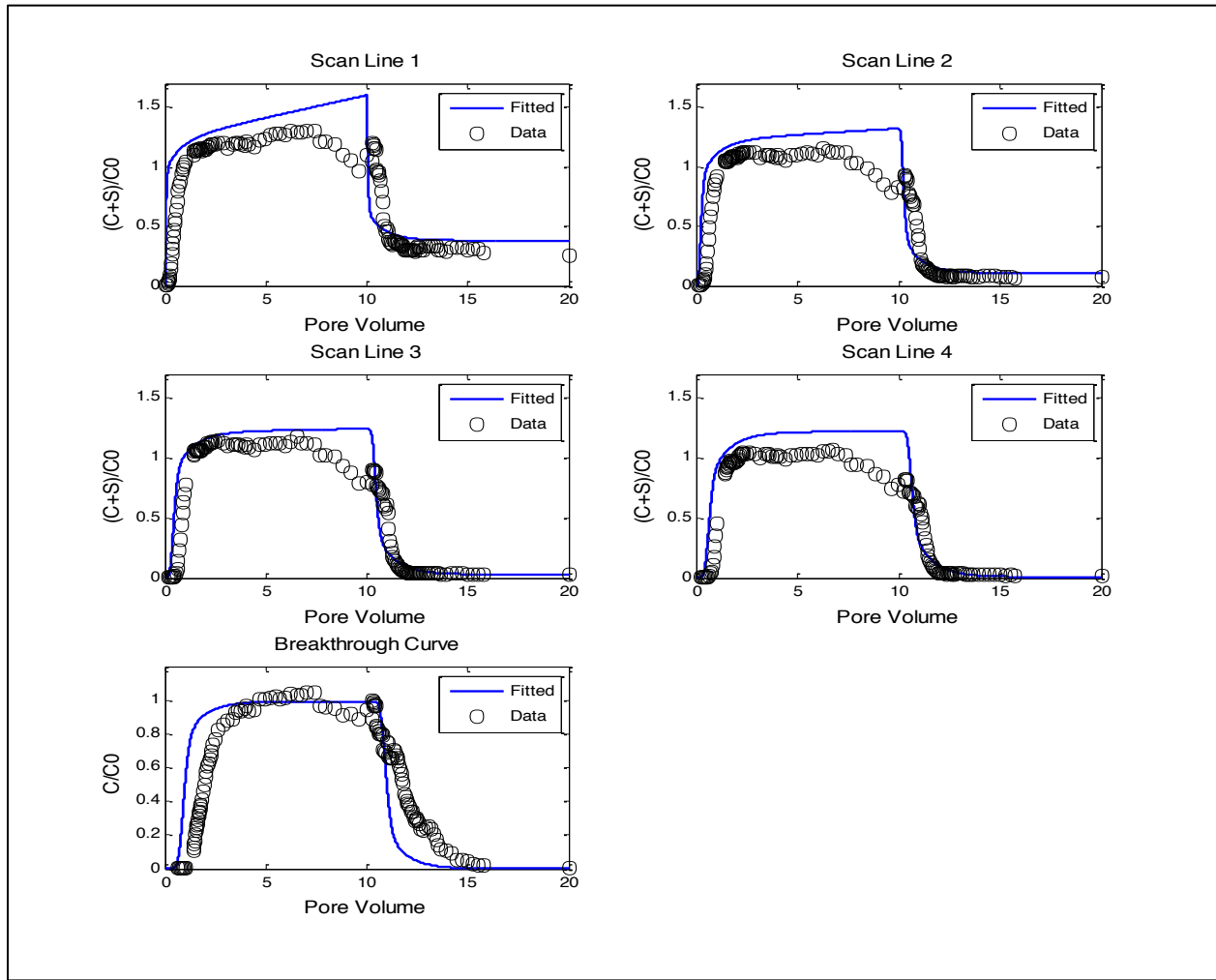


Figure 19. Simulated 1-um particle transport via dual mode model. Comparing with the 1-site irreversible, reversible, and 2-site kinetic model, the dual mode model effectively fitted measured data with reasonable matching of the peak concentration and tails of all scan-lines.

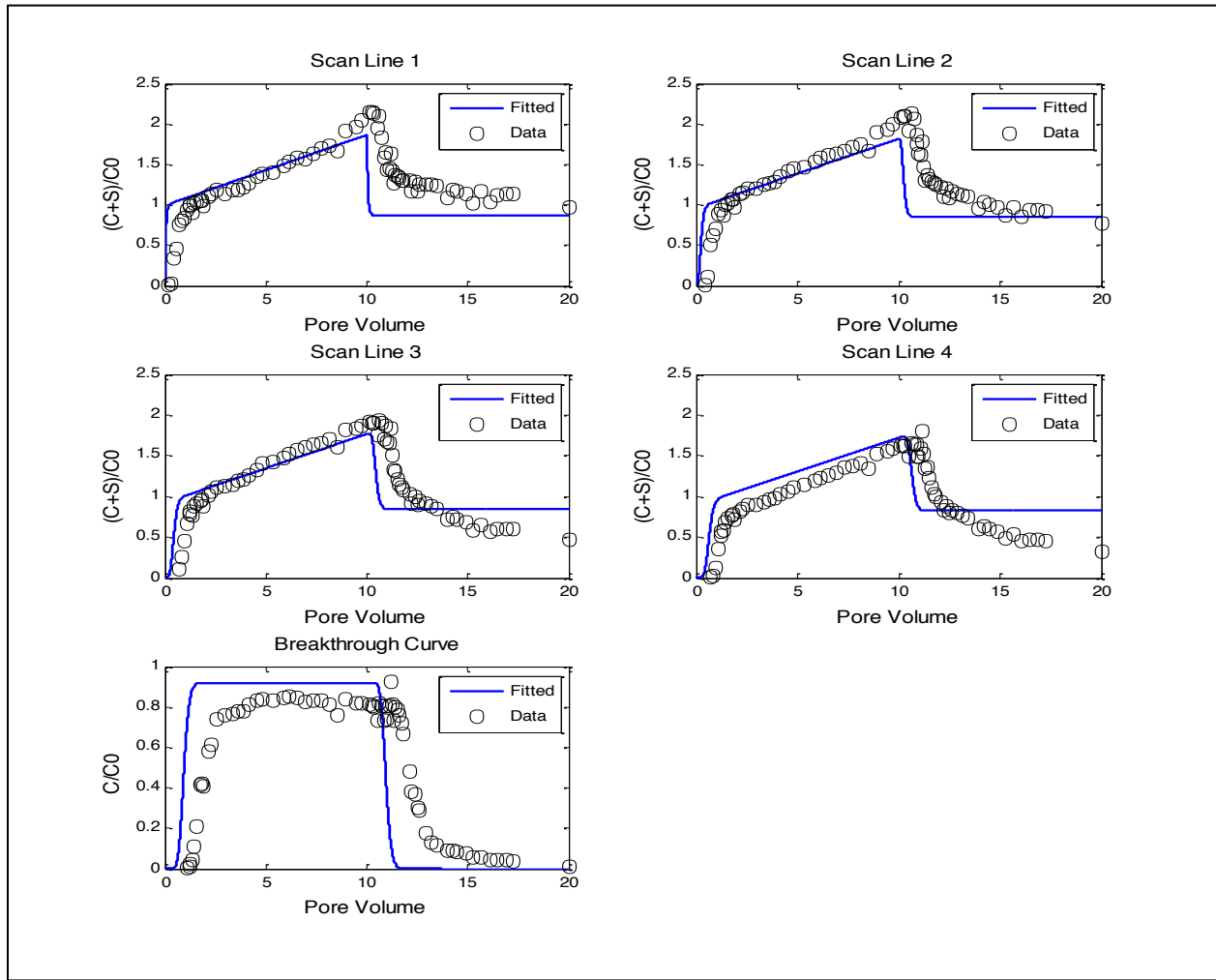


Figure 20. Simulated 3-um particle transport via 1-site irreversible attachment model. Results indicate that the irreversible model can fit the measured data with respect to peak concentration. However, the model does not capture the overall shape of the particle concentration curves.

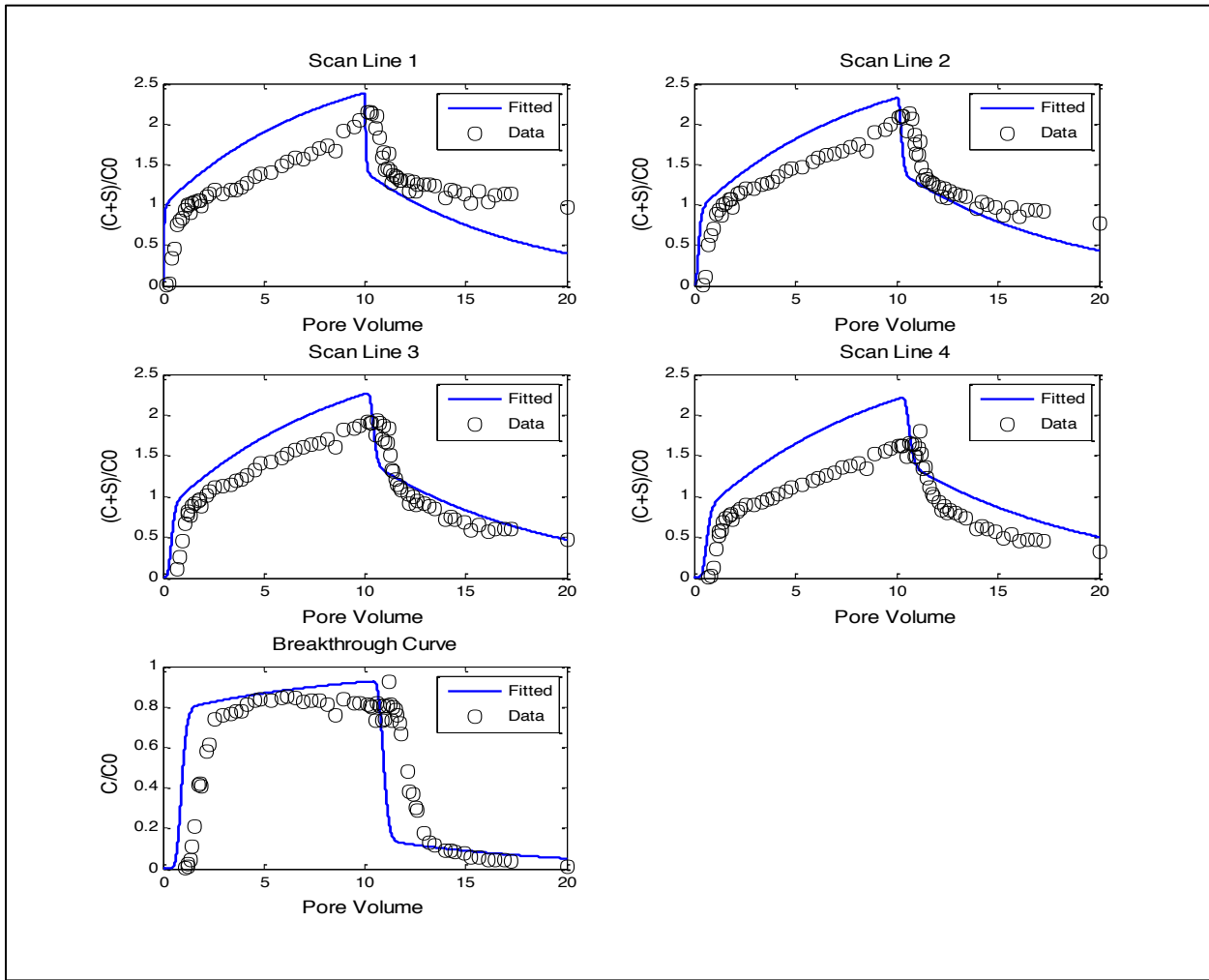


Figure 21. Simulated 3-um particle transport via 1-site reversible attachment and detachment model. Results showed that reversible model improves fitting with respect to the irreversible model. However, the reversible model cannot fit the final retained concentrations very well.

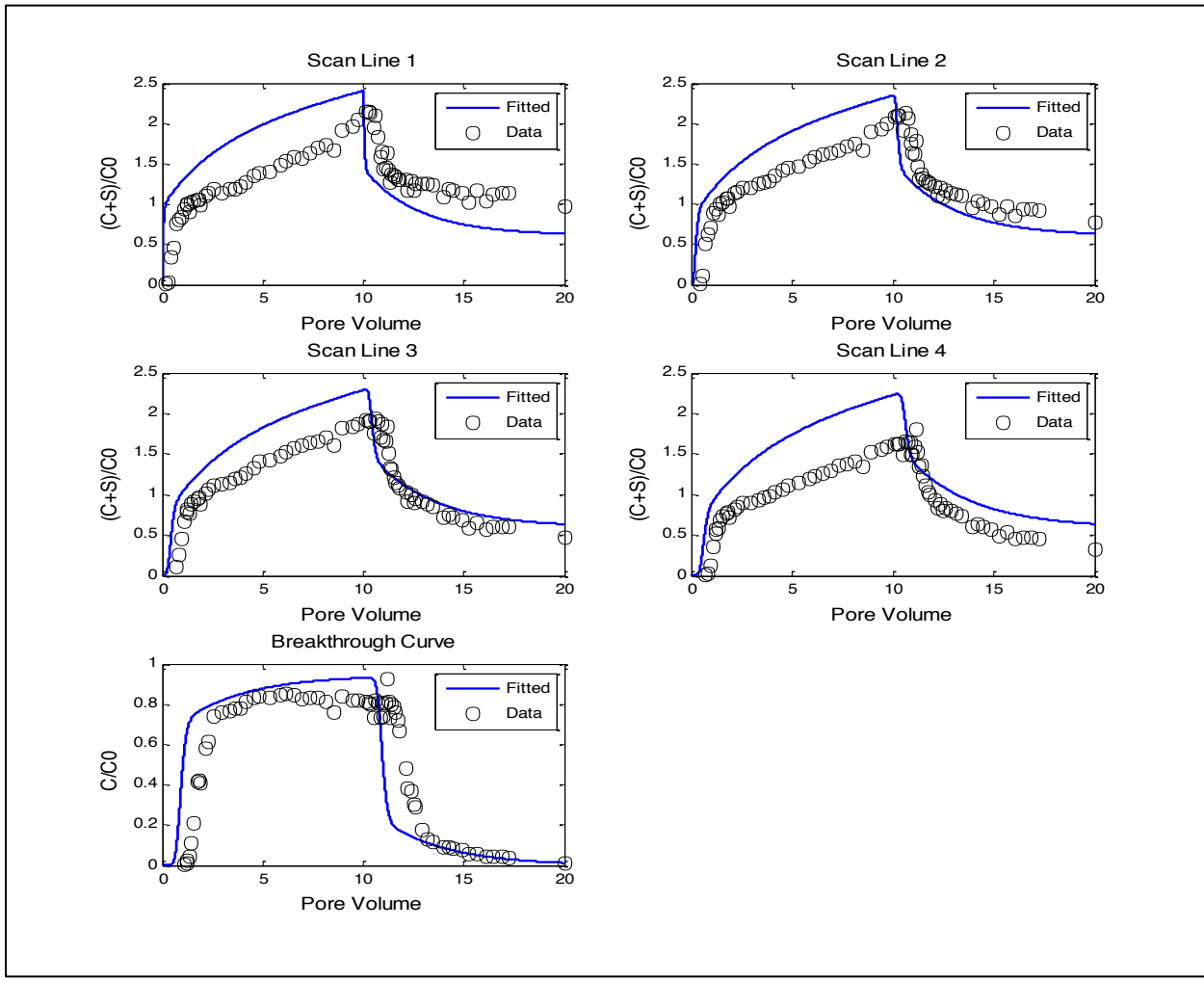


Figure 22. Simulated 3-um particle transport via 2-site kinetic model. Results show that the 2-site model improves the tails fits of all scan-lines and the breakthrough curve, especially the transition time (around 10 pore volumes). However, the 2-site model cannot fit the final retained concentration.

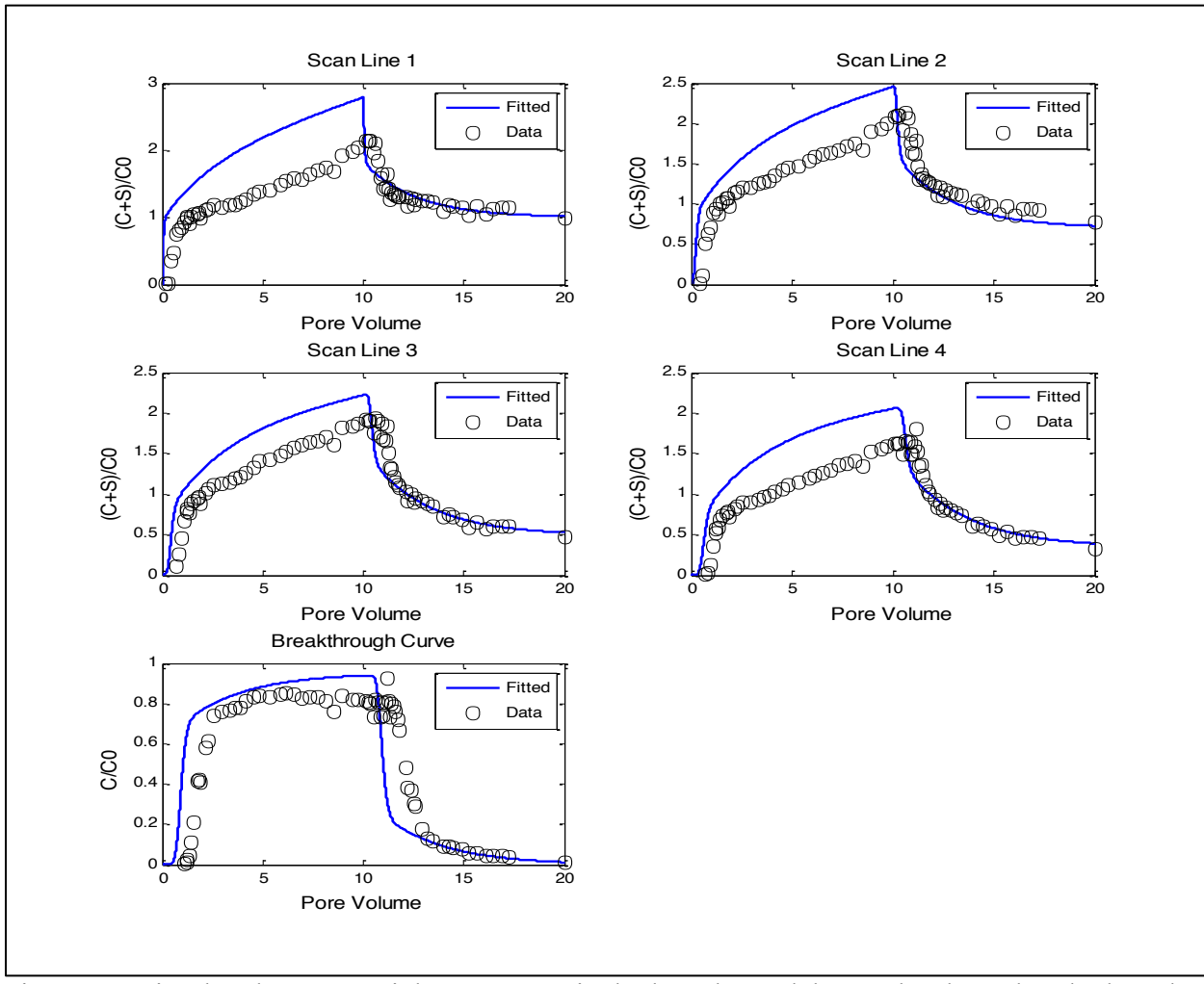


Figure 23. Simulated 3-um particle transport via dual mode model. Results show that dual mode model can fit the tails of all scan-lines, breakthrough curves, and the final retained concentration simultaneously. Nonetheless, the dual mode model overestimated peak concentrations, which resulted in a large residual.

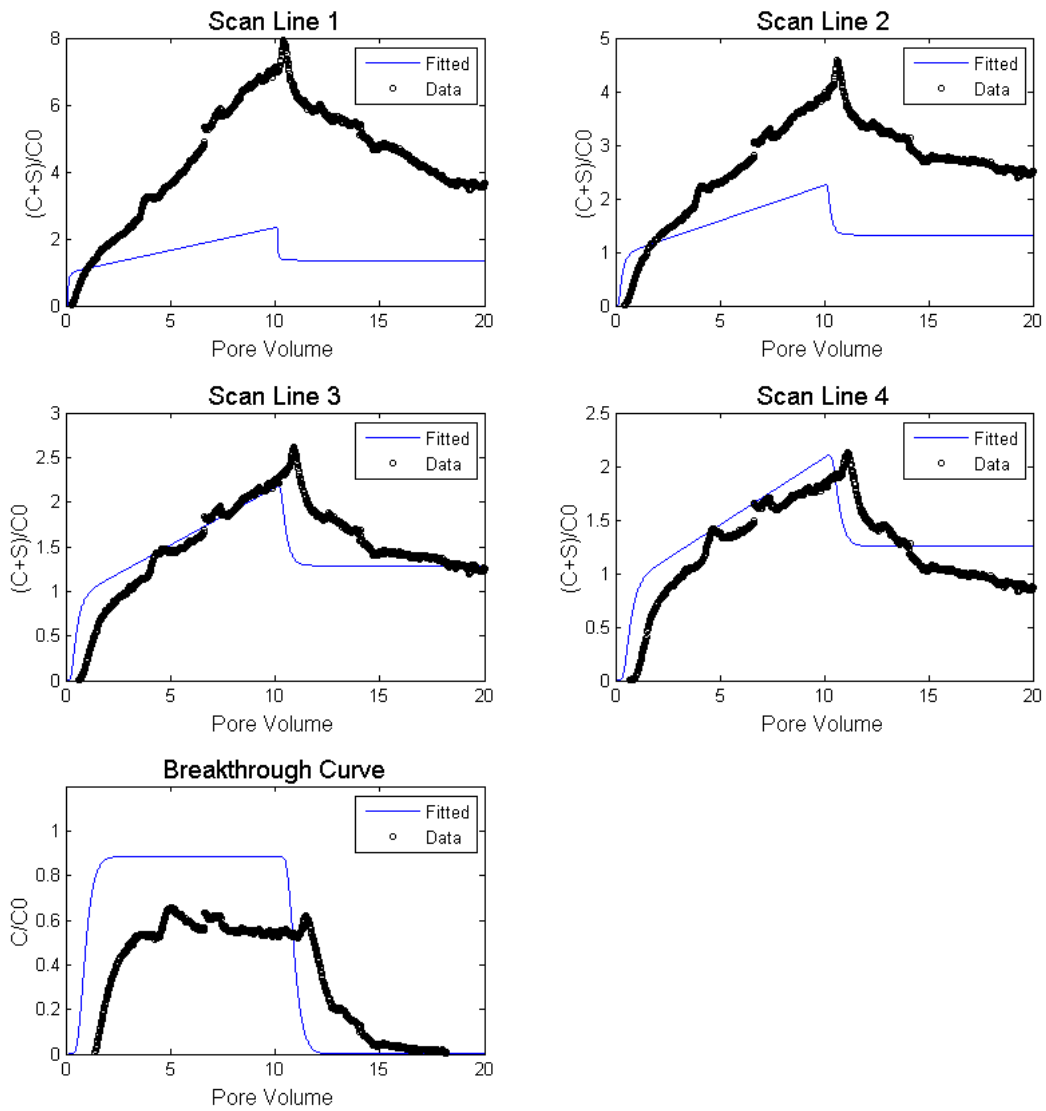


Figure 24. Simulated 6- μm particle transport via 1-site irreversible attachment model. Comparison shows that the irreversible model cannot fit the measured data. The model can only fit scan-line 3 and 4 peaks, it underestimates scan-line 1 and 2 concentrations, and overestimates the breakthrough concentration.

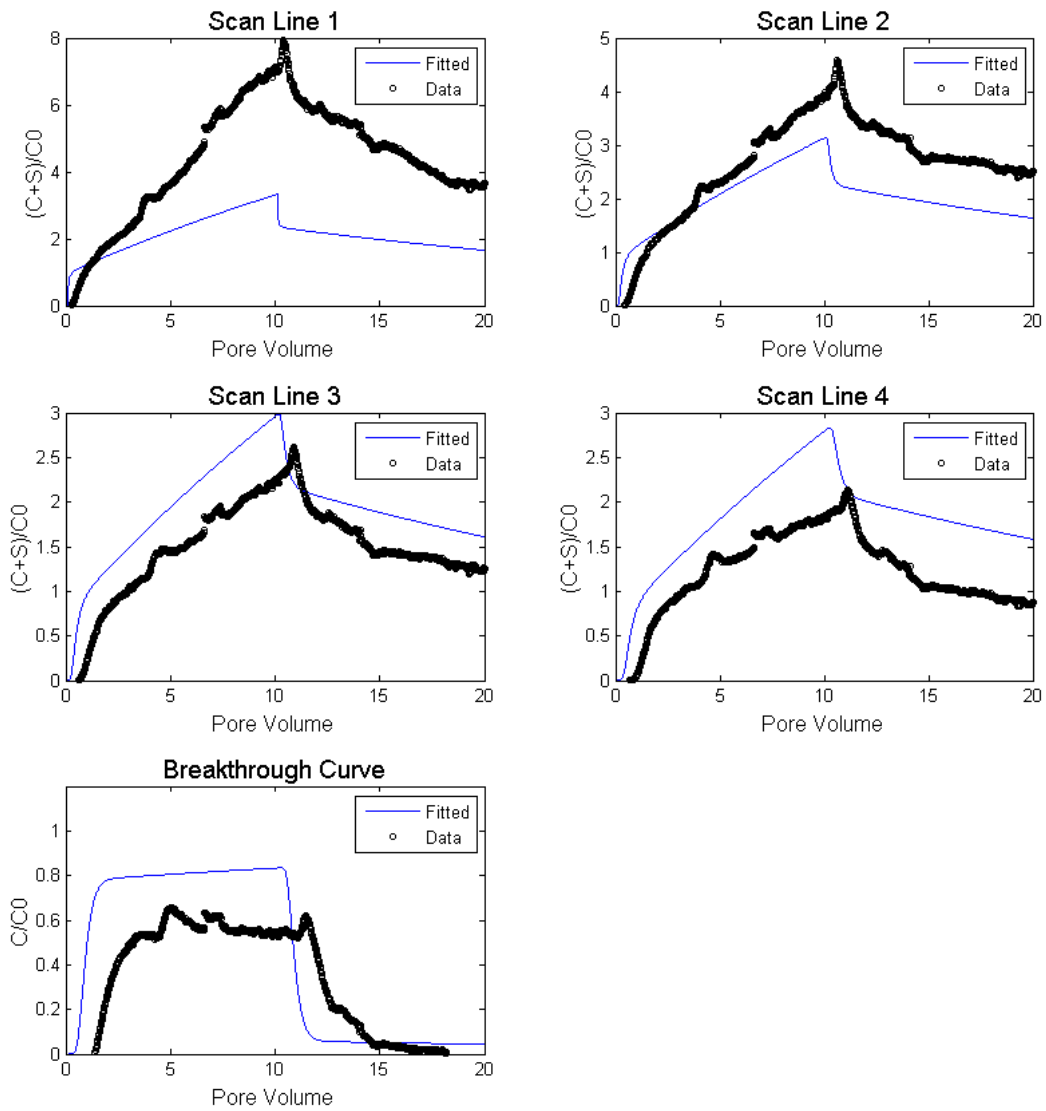


Figure 25. Simulated 6- μm particle transport via 1-site reversible attachment model. Comparison shows that the reversible model can predict experimental curves for scan-lines 3 and 4. However, the reversible model underestimated scan-line 1 and 2 concentrations and overestimated breakthrough concentrations.

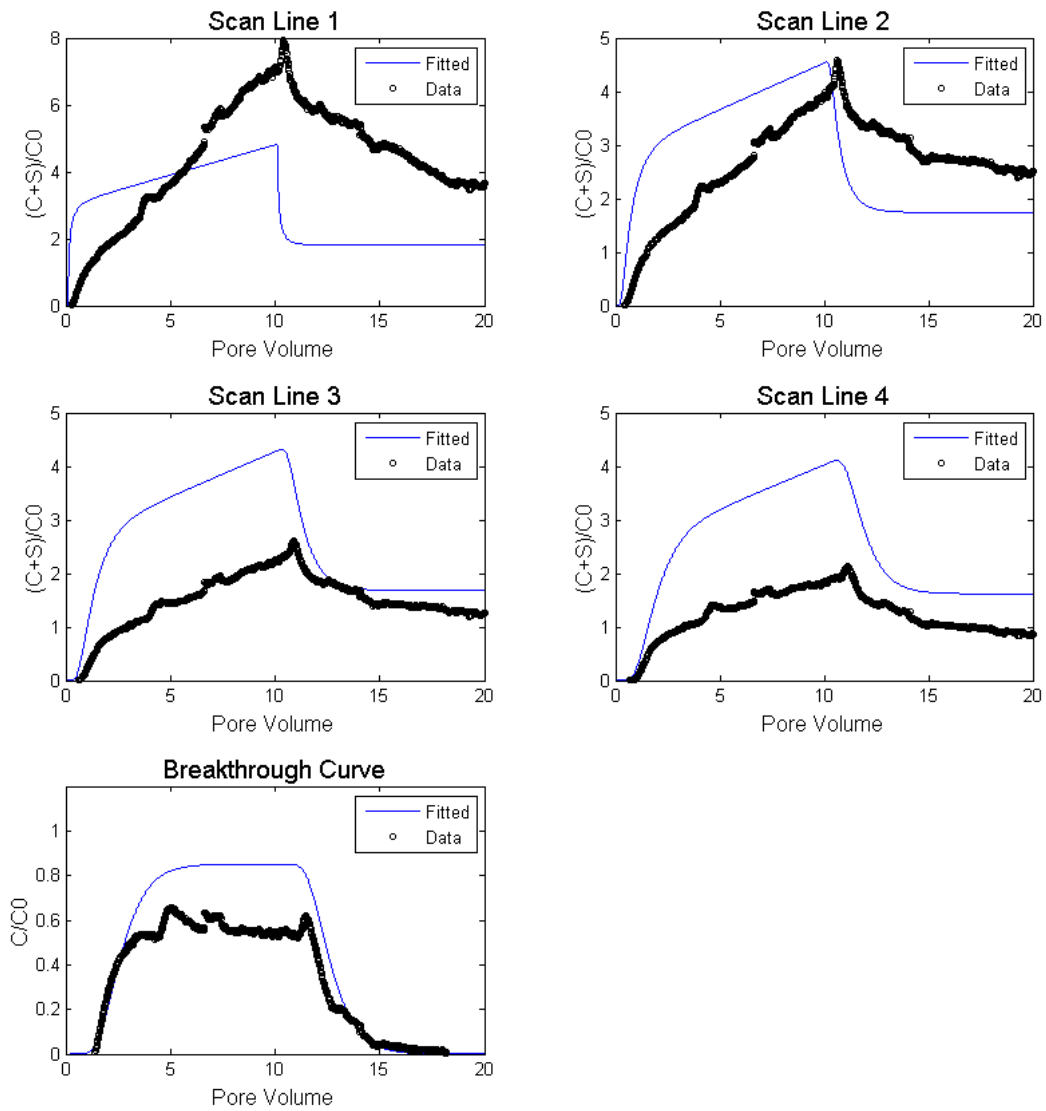


Figure 26. Simulated 6-um particle transport via the 2-site attachment model. Comparison shows that the 2-site model improved scan-line 1, 2 and breakthrough fitting results. The modeled breakthrough curve presented similar trends with observed data. However, the model cannot fit scan-line 3 and 4 simultaneously. The 2-site model overestimated scan-line 3 and 4 concentrations.

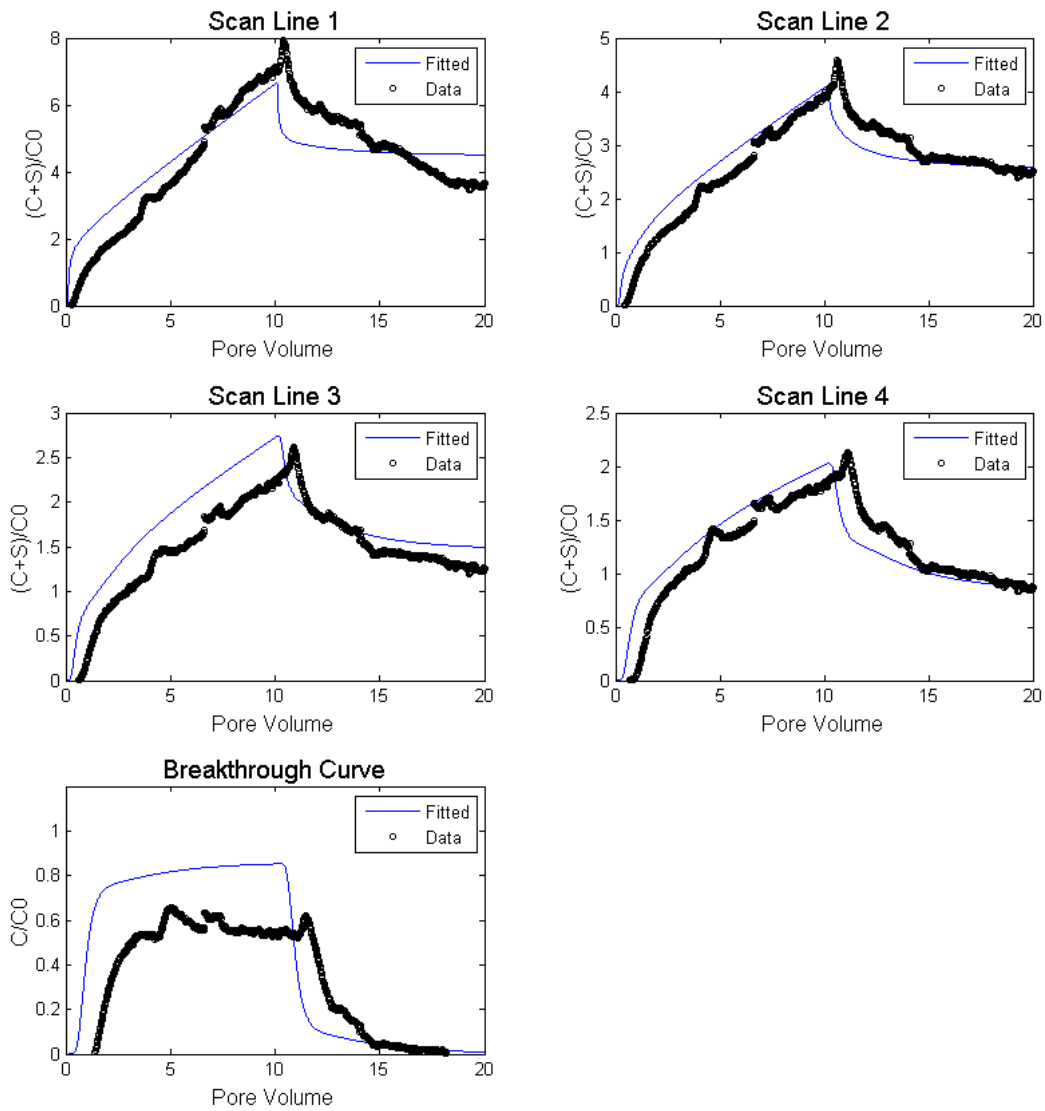


Figure 27. Simulated 6-um particle transport via the dual mode model. Comparison shows that the dual mode model can fit measured data with respect to peak concentration and tails for all scan-lines. However, the model overestimated the breakthrough concentration.

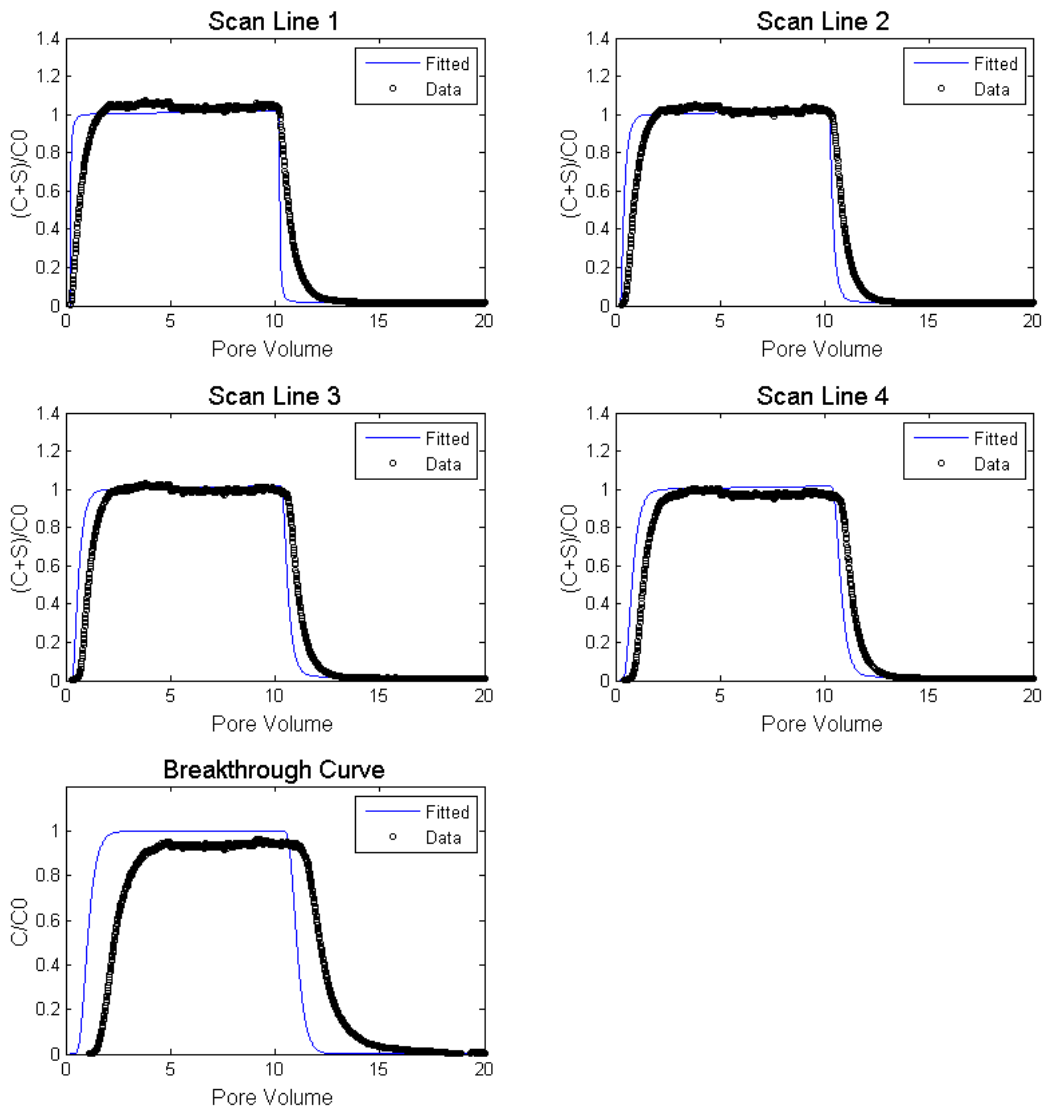


Figure 28. Simulated 1-um with 6-um particles transport via 1-site irreversible attachment model. Comparison shows that the irreversible model can fit measured data with respect to peak concentration. However, the model does not fit the lag time of the experiment.

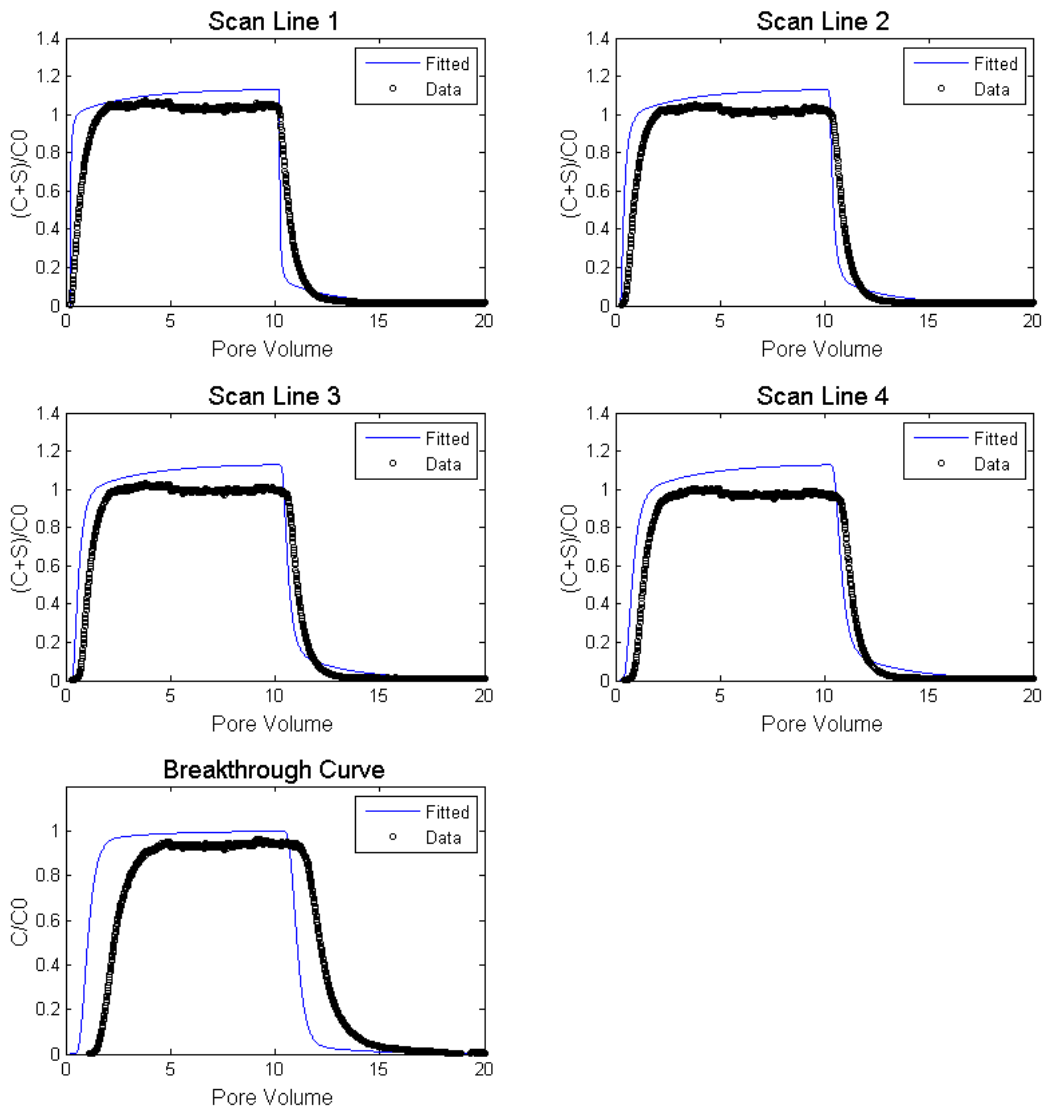


Figure 29. Simulated 1-um particle with 6-um particle present transport via 1-site reversible attachment model. Comparison shows that the reversible model can fit scan-lines' 1 to 4 decreasing trend better than the irreversible model. However, the reversible model slight overestimates the plateau concentration.

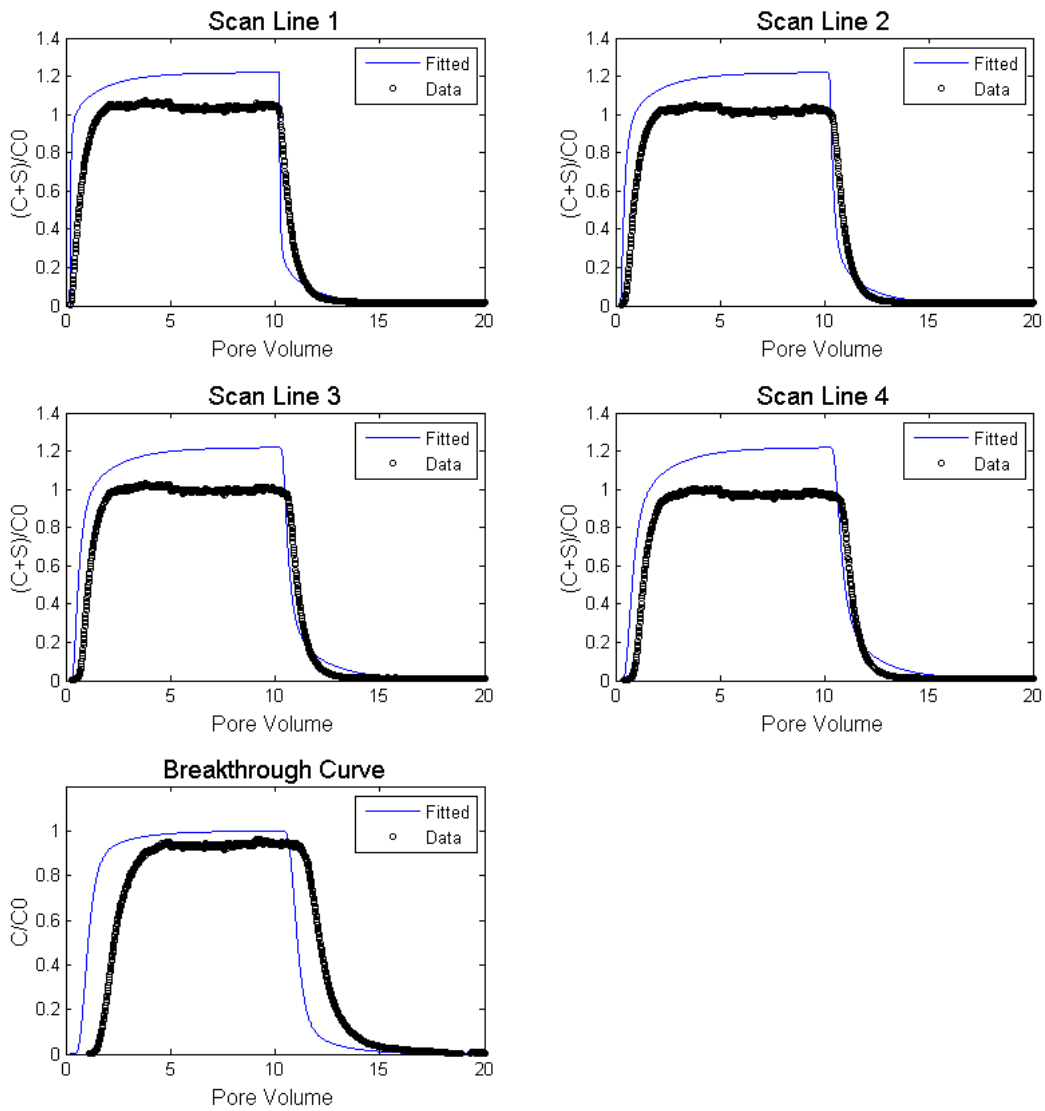


Figure 30. Simulated 1-um particle with 6-um particle present transport via 2-site model. Comparison shows that the 2-site model can fit scan-line tails better and present similar trends for the measured breakthrough curve. However, the model overestimated scan-line plateau concentrations.

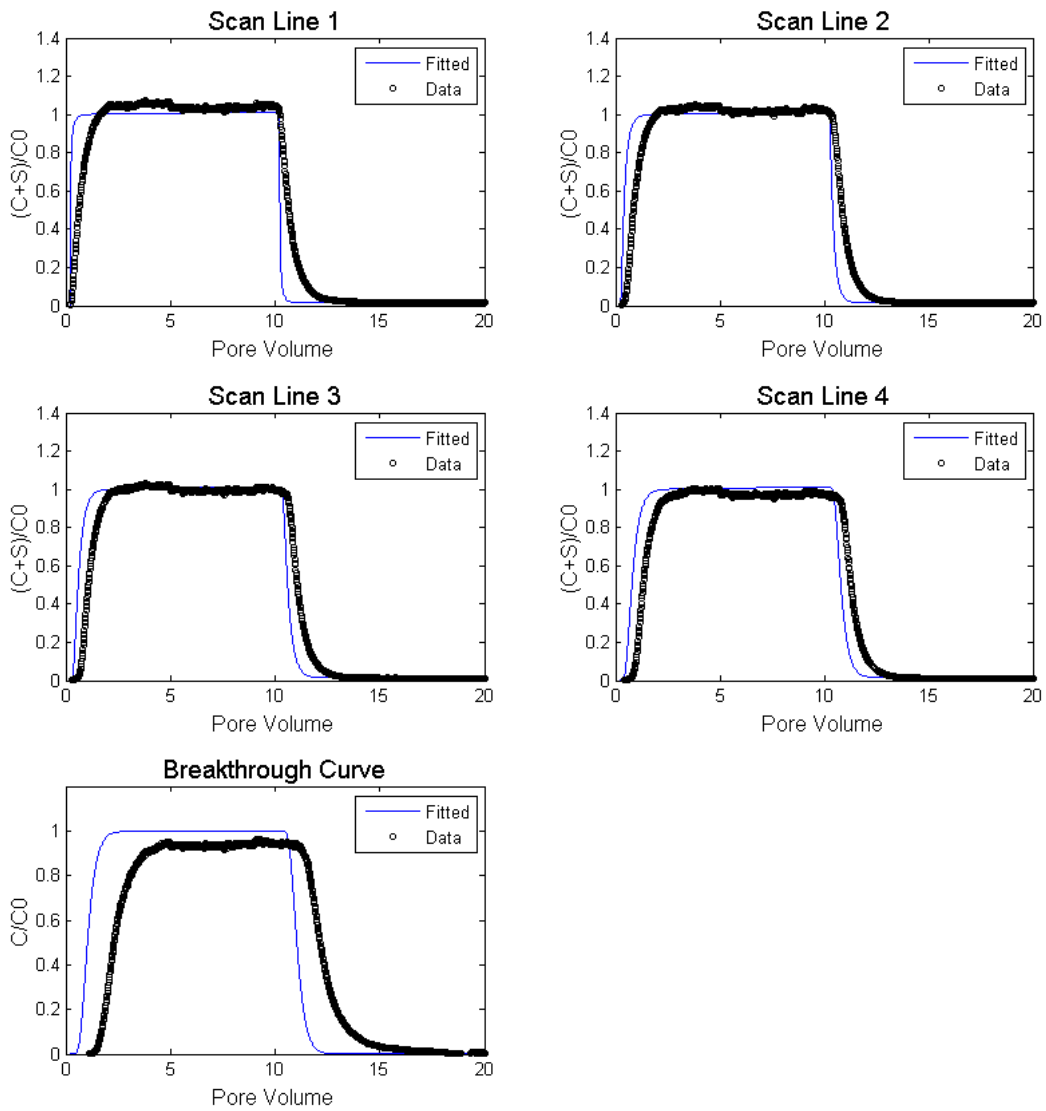


Figure 31. Simulated 1-um particle with 6-um particle present transport via dual mode model. The comparison shows that the dual mode model converged to irreversible model, and thus presented similar results.

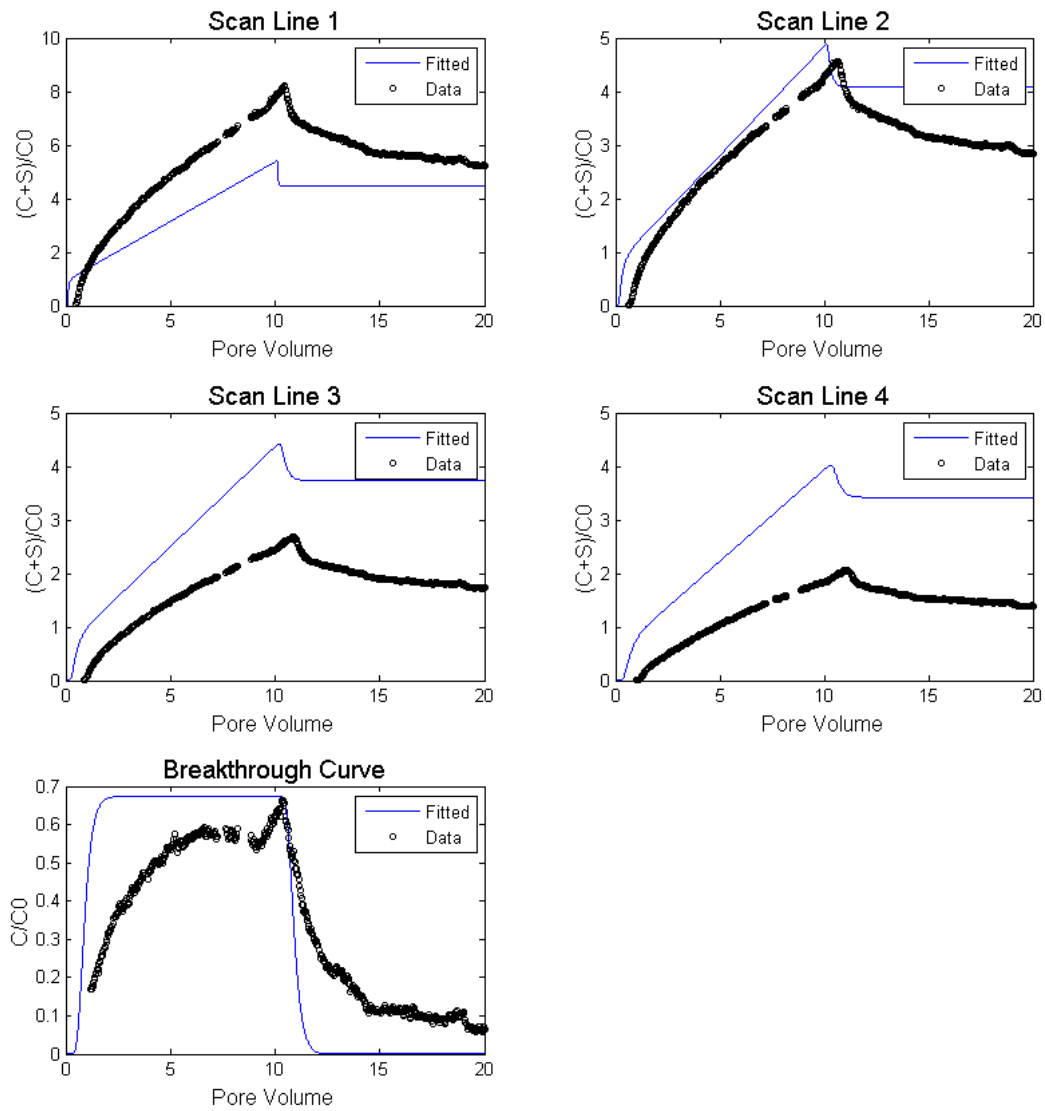


Figure 32. Simulated 6-um particle with 1-um particle present via the 1-site irreversible model. Comparison shows that the irreversible model cannot fit measured data. The model underestimated scan-line 1 and overestimated all scan-line 3 and 4 concentrations.

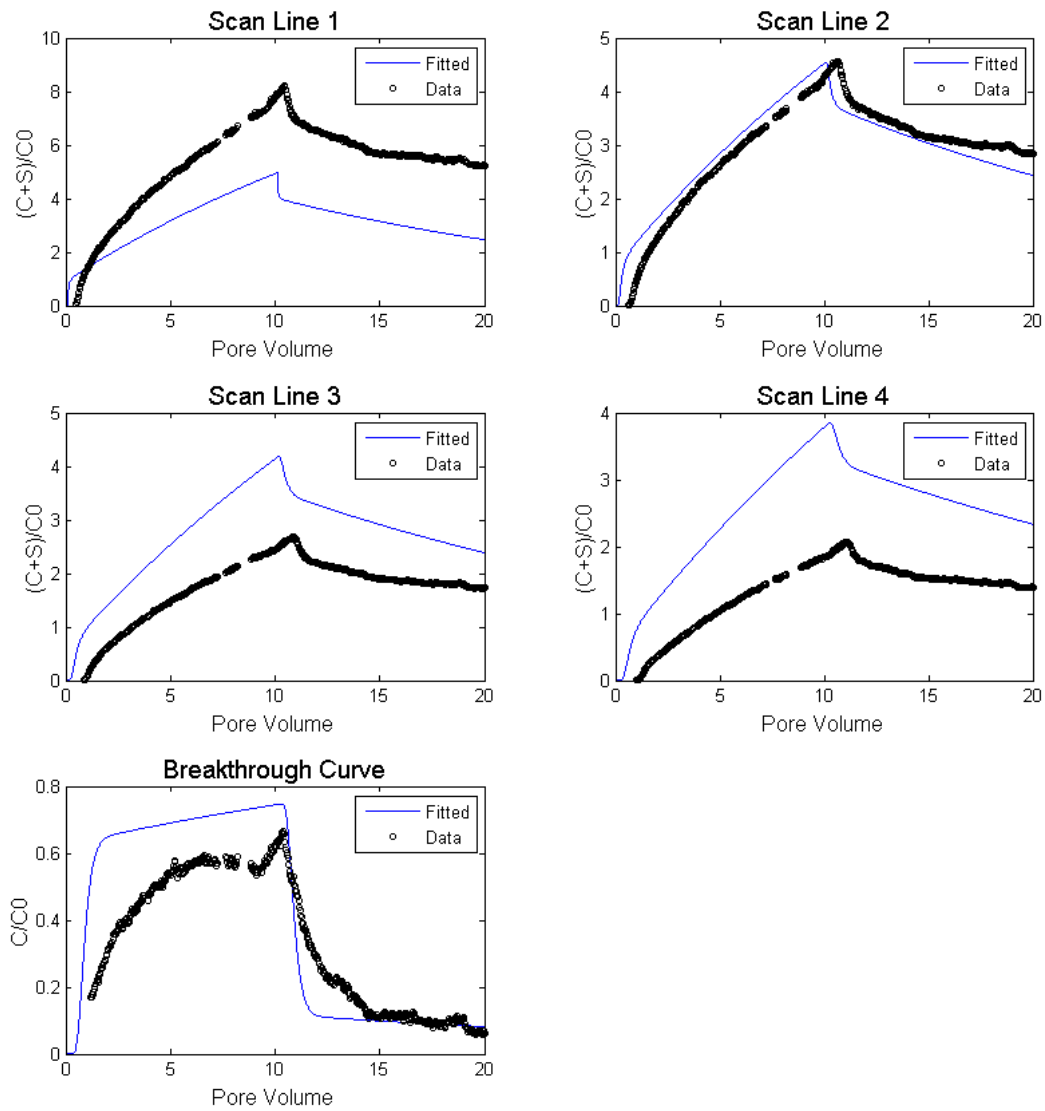


Figure 33. Simulated 6-um particle with 1-um particle present transport via the 1-site reversible attachment model. The model can predict similar scan-line concentrations (e.g., scan-line 2 as shown here). However, the model still cannot fit all scan-lines simultaneously.

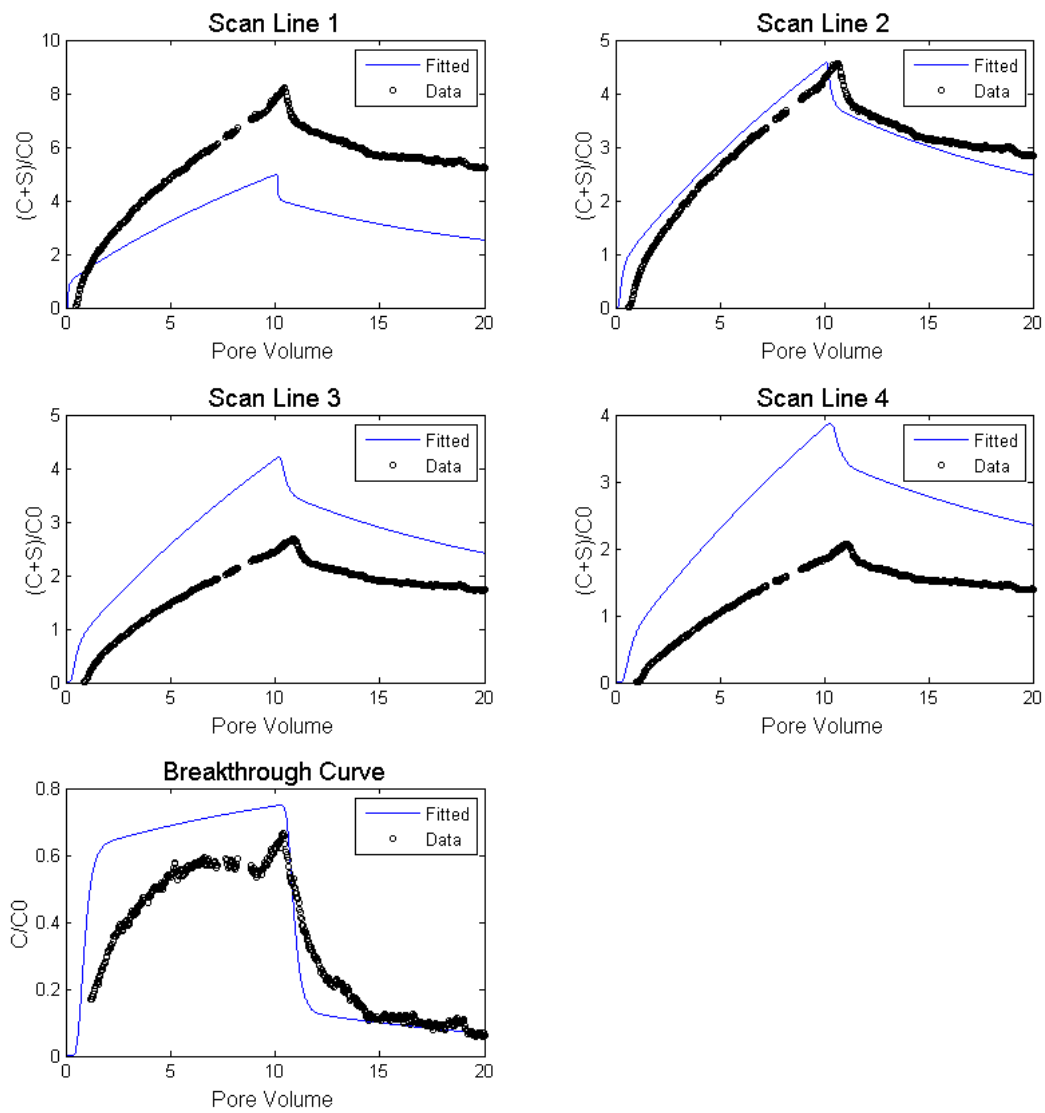


Figure 34. Simulated 6-um particle with 1-um particle present transport via 2-site model. In this case, the 2-site model presents similar simulation results as the reversible model.

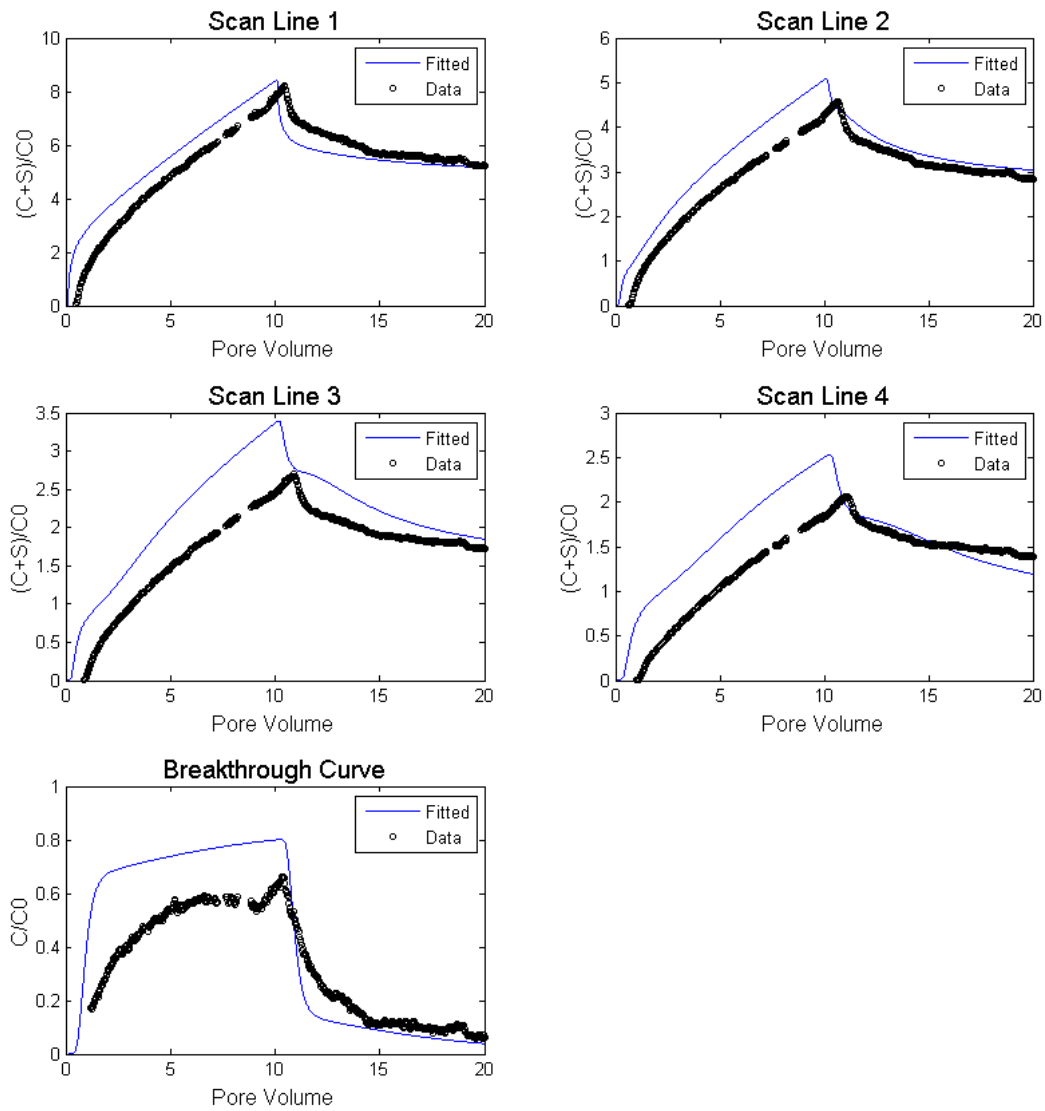


Figure 35. Simulated 6-um particle with 1-um particle present transport via the dual mode model. The dual mode model provided the best simulation results. Simulated scan-lines presented similar trends to the observed data. The model slightly overestimated scan-lines 3, 4, and the breakthrough concentrations.

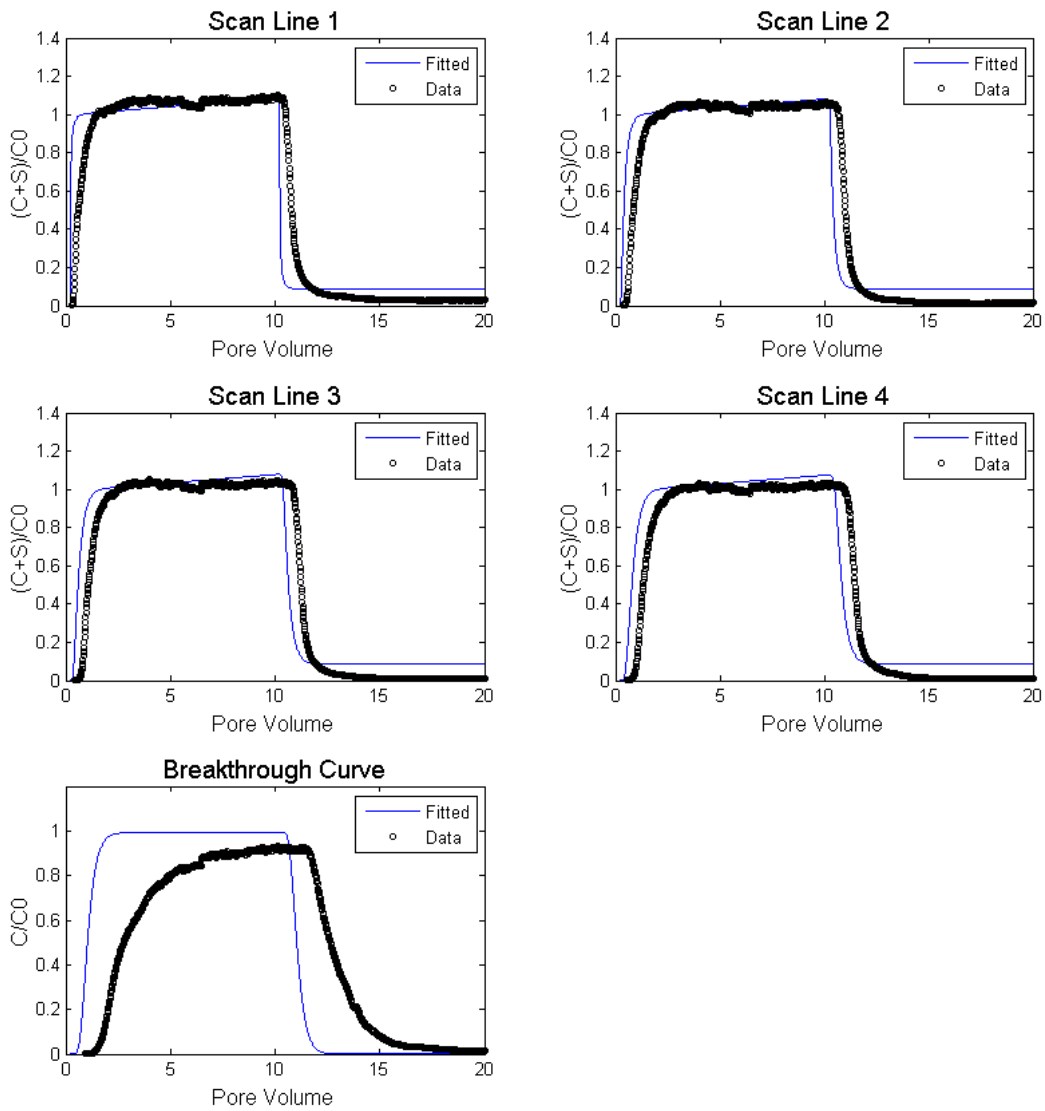


Figure 36. Simulated 1-um particle transport with upward flow condition via 1-site irreversible attachment model. The irreversible model can fit measured scan-lines well. However, the breakthrough curve presented a totally different trend compared with downward flow conditions. The irreversible model cannot fit the breakthrough curve's increasing trend.

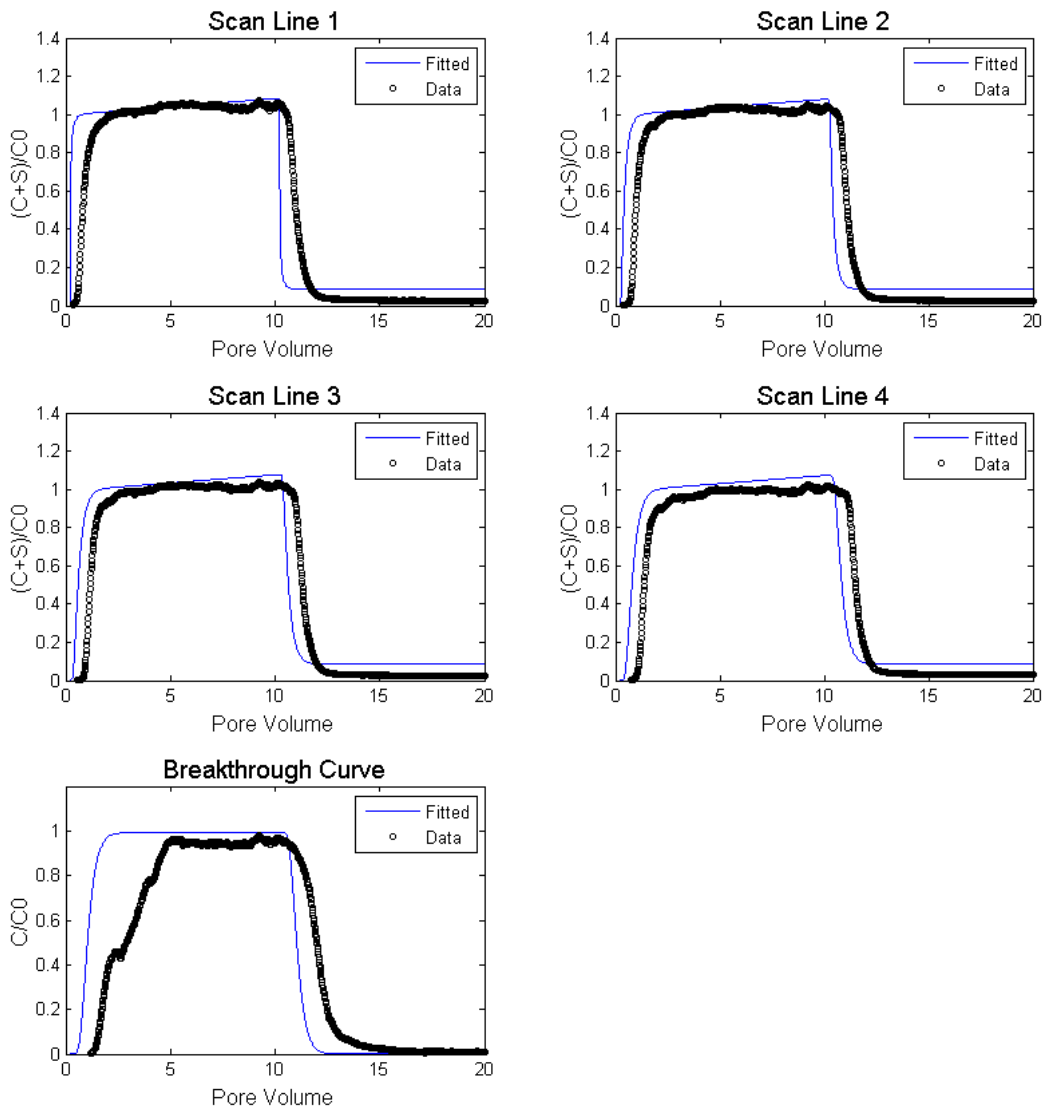


Figure 37. Simulated 1-um particle transport with horizontal flow conditions via the 1-site irreversible attachment model. The irreversible model fitted measured scan-lines plateaus well, but slightly overestimated tail concentrations. The irreversible model could not fit the breakthrough curves increasing trend.

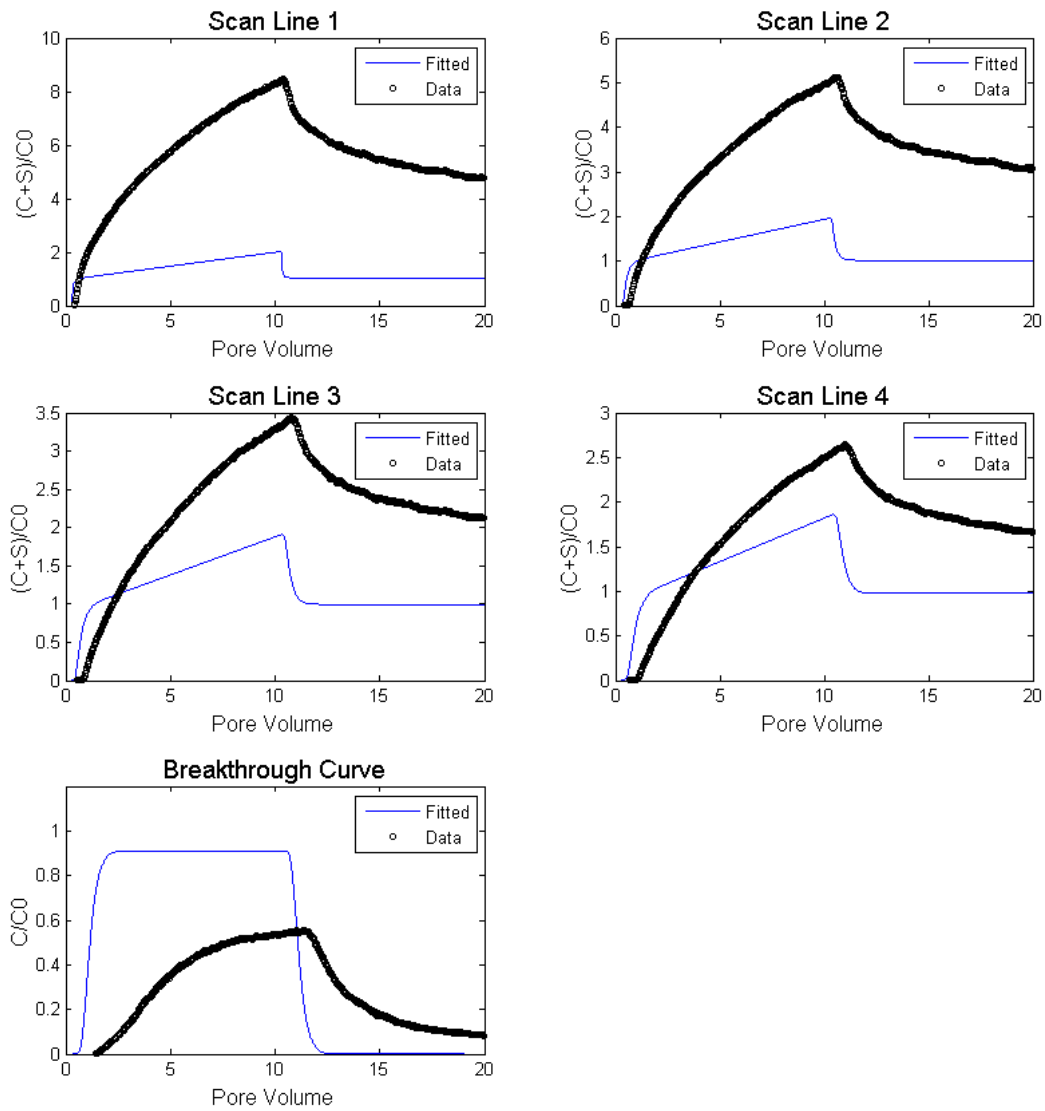


Figure 38. Simulated 6-um particle transport with upward flow conditions via 1-site irreversible attachment model. 6-um breakthrough curve presented similar increasing trends to the 1-um particle transport with upward flow conditions. The irreversible model cannot fit the scan-line data nor the breakthrough curve data.

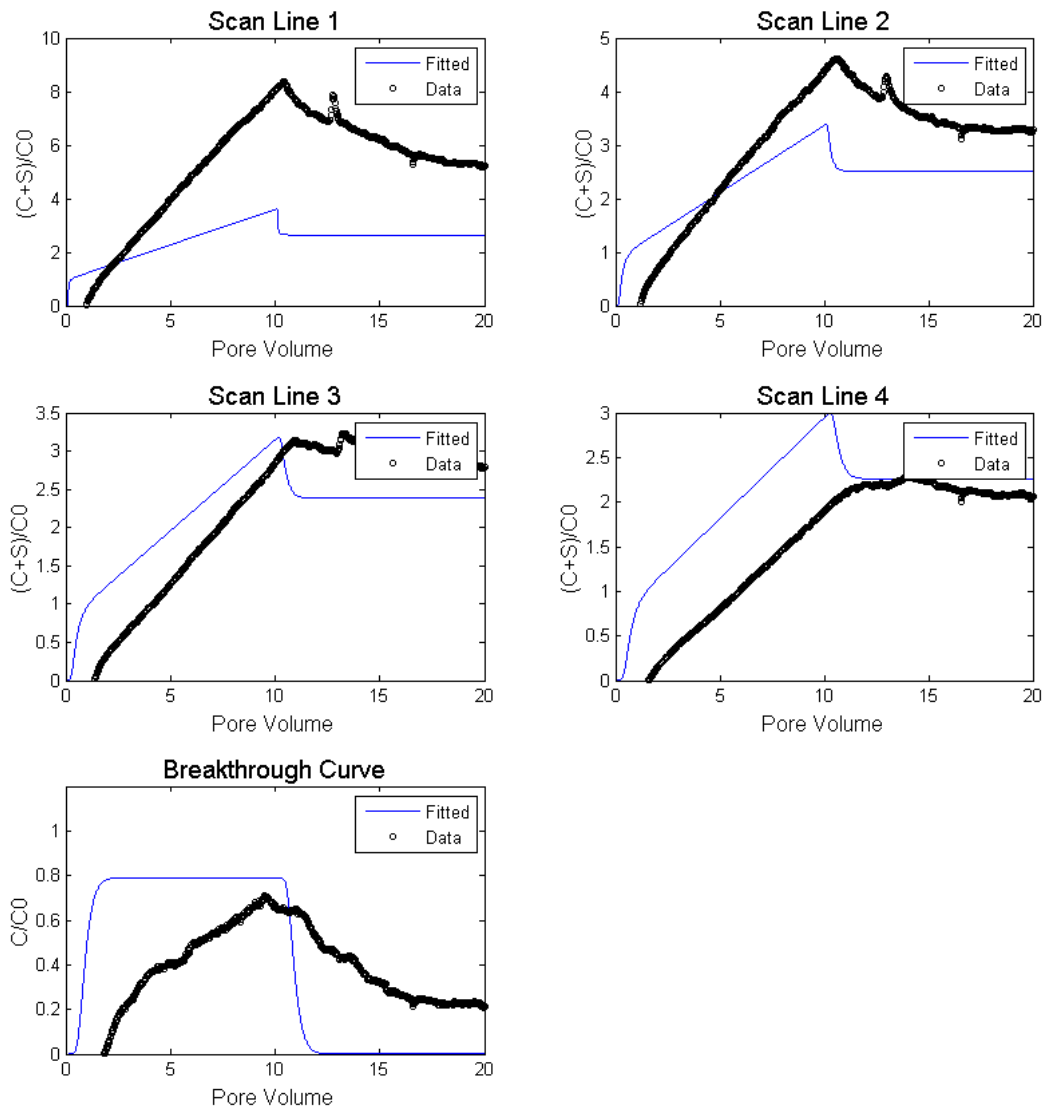


Figure 39. Simulated 6-um particle transport with horizontal flow conditions via the 1-site irreversible attachment model. Under horizontal flow conditions, the 6-um transport experiment presented different increasing and decreasing trends comparing with the tests conducted under downward and upward flow conditions. The irreversible model cannot fit the steep increasing and mild decreasing trends observed in the 6-um horizontal test.

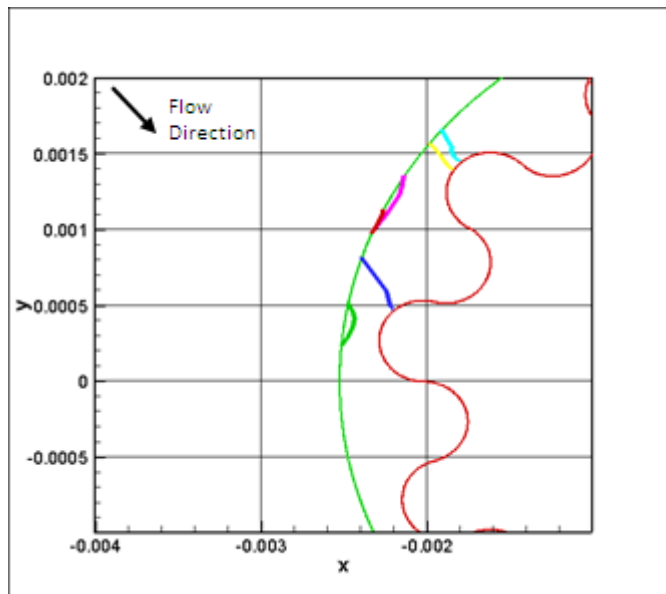


Figure 40. Trajectories followed by a number of particles obtained during the simulations for the flow with an approach velocity of $5.49 \cdot 10^{-4}$ m/sec at an angle of -45° to the x -axis

Table 1. Experimental conditions of column experiments and irreversible attachment rates estimated from plateaus of column BTCs. Ionic strength for experiments was 3.5 mM apart from experiment C4 which was set at 20 mM.

Experimental condition	Collector size (mm)	Particle size (um)	Velocity (cm/s)	Flow direction	Kirr (s)
J1	4	1-25	5.5×10^{-2}	D	1.48×10^{-4}
J2	4	1-25	2.7×10^{-2}	D	2.25×10^{-4}
J3	4	1-25	1.4×10^{-2}	D	2.36×10^{-4}
A1	0.5	1-25	2.0×10^{-3}	D	1.00×10^{-3}
A2	0.5	1-25	2.0×10^{-3}	U	9.24×10^{-4}
A3.1 soleA	0.5	1	2.0×10^{-3}	D	6.15×10^{-5}
A3.2 soleB	0.5	1	2.0×10^{-3}	D	1.19×10^{-5}
A4	0.5	3	2.0×10^{-3}	D	1.03×10^{-4}
A5.1	0.5	6	2.0×10^{-3}	D	1.11×10^{-3}
A5.2	0.5	6	2.1×10^{-3}	D	7.97×10^{-4}
A6	0.5	6 with 1 present	2.0×10^{-3}	D	1.13×10^{-4}
A7	0.5	1 with 6 present	2.0×10^{-3}	D	7.34×10^{-6}
C1	0.5	1	2.0×10^{-3}	H	6.00×10^{-5}
C2	0.5	1	2.0×10^{-3}	U	5.49×10^{-5}
C3	0.5	1	2.0×10^{-3}	D	3.78×10^{-5}
C4	0.5	1	2.0×10^{-3}	D	4.25×10^{-4}
<hr/>					
D1	0.5	1	2.0×10^{-3}	D	$1.72E-06$
D2	0.5	1	2.0×10^{-3}	D	$8.01E-07$
D3	0.5	1 with 6 present	2.0×10^{-3}	D	$1.01E-06$
D4	0.5	1 with 6 present	2.0×10^{-3}	D	$2.11E-06$
D5	0.5	6	2.0×10^{-3}	D	$7.16E-05$
D6	0.5	6	2.0×10^{-3}	D	$1.90E-04$
D7	0.5	6 with 1 present	2.0×10^{-3}	D	$2.33E-04$
D8	0.5	6 with 1 present	2.0×10^{-3}	D	$1.50E-04$
U1	0.5	1	2.0×10^{-3}	U	$2.43E-06$
U2	0.5	1	2.0×10^{-3}	U	$3.76E-06$
U3	0.5	1 with 6 present	2.0×10^{-3}	U	$2.96E-06$
U4	0.5	1 with 6 present	2.0×10^{-3}	U	$4.52E-06$
U5	0.5	6	2.0×10^{-3}	U	$7.53E-03$
U6	0.5	6	2.0×10^{-3}	U	$2.25E-03$
U7	0.5	6 with 1 present	2.0×10^{-3}	U	$4.68E-03$
U8	0.5	6 with 1 present	2.0×10^{-3}	U	$5.36E-03$
H1	0.5	1	2.0×10^{-3}	H	$2.43E-06$
H2	0.5	1	2.0×10^{-3}	H	$9.25E-06$
H3	0.5	6	2.0×10^{-3}	H	$1.37E-04$
H4	0.5	6	2.0×10^{-3}	H	$3.48E-04$

Table 2. Summary of parameters estimated from fitting the macroscopic, kinetic model to results from column experiments

		1st Population			2nd Population		
1-um Particle	Proportion	k_i (sec $^{-1}$)	k_a (sec $^{-1}$)	k_d (sec $^{-1}$)	Proportion	k_i (sec $^{-1}$)	Residual
Irreversible Model	1	3.95E-06	NA	NA	NA	NA	29.35
Reversible Model	1	NA	3.94E-05	7.66E-05	NA	NA	3.73
Two Site Model	1	2.08E-06	1.27E-04	2.20E-04	NA	NA	3.55
Dual Mode Model	0.99	0.00E+00	5.40E-05	2.40E-04	0.01	1.50E-03	3.38
3-um Particle	Proportion	k_i (sec $^{-1}$)	k_a (sec $^{-1}$)	k_d (sec $^{-1}$)	Proportion	k_i (sec $^{-1}$)	Residual
Irreversible Model	1	2.36E-05	NA	NA	NA	NA	39.08
Reversible Model	1	NA	3.35E-05	1.13E-05	NA	NA	4.02
Two Site Model	1	6.08E-05	7.35E-05	1.23E-05	NA	NA	3.94
Dual Mode Model	0.94	4.55E-04	6.75E-05	7.78E-05	0.06	3.70E-04	3.75
6-um Particle	Proportion	k_i (sec $^{-1}$)	k_a (sec $^{-1}$)	k_d (sec $^{-1}$)	Proportion	k_i (sec $^{-1}$)	Residual
Irreversible Model	1	7.16E-05	NA	NA	NA	NA	55.4
Reversible Model	1	NA	8.45E-05	1.84E-05	NA	NA	6.45
Two Site Model	1	9.33E-05	1.66E-04	8.03E-05	NA	NA	8.06
Dual Mode Model	0.85	1.77E-04	8.69E-04	1.33E-04	0.15	9.07E-04	3.20
1-um with 6-um Particle	Proportion	k_i (sec $^{-1}$)	k_a (sec $^{-1}$)	k_d (sec $^{-1}$)	Proportion	k_i (sec $^{-1}$)	Residual
Irreversible Model	1	1.01E-06	NA	NA	NA	NA	7.09
Reversible Model	1	NA	4.51E-05	1.87E-04	NA	NA	1.03
Two Site Model	1	4.37E-07	7.46E-04	3.52E-04	NA	NA	0.93
Dual Mode Model	1	1.01E-06	0	0	0	0	7.09
6-um with 1-um Particle	Proportion	k_i (sec $^{-1}$)	k_a (sec $^{-1}$)	k_d (sec $^{-1}$)	Proportion	k_i (sec $^{-1}$)	Residual
Irreversible Model	1	2.33E-04	NA	NA	NA	NA	252.1
Reversible Model	1	NA	2.65E-04	2.57E-05	NA	NA	6.48
Two Site Model	1	7.81E-05	2.03E-04	4.79E-05	NA	NA	6.47
Dual Mode Model	0.83	1.80E-04	1.41E-04	8.92E-05	0.17	5.57E-04	3.59

Table 3. System parameters used for particle tracking

Parameter	Value (Range)	Parameter	Value (Range)
Particle radius, r_p	$1\text{--}12.5\cdot10^{-6}$ m	Boltzmann constant, k	$1.38\cdot10^{-23}$ J/K
Average collector radius, r_c	$2\cdot10^{-3}$ m	Absolute temperature, T	293 K
Porosity, n	0.376	Zeta potential of particle, ζ_p	-110 miliVolt
Particle density, ρ_p	991 kg/m ³	Zeta potential of collector, ζ_c	-60 miliVolt
Fluid density, ρ_f	$1100\text{--}1500$ kg/m ³	Electronic charge, e	$1.6\cdot10^{-19}$ c
Fluid dynamic viscosity, μ	$9.98\cdot10^{-6}$ kg/m/sec	Cation valance, z_{ce}	2
Separation distance, h	$1\cdot10^{-6}$ m	Molar concentration of cations, C_0	$1\cdot10^{-5}$ moles
Hamaker constant, H	$1\cdot10^{-19}$ J	Dielectric constant of fluid, D	80

Table 4. Variables investigated for particle tracking work

Approach Velocity (m/sec)	$v_x = 0$ $v_y = -5.49\cdot10^{-4}$	$v_x = 0$ $v_y = -2.76\cdot10^{-4}$	$v_x = 0$ $v_y = -1.38\cdot10^{-4}$	$v_x = 5.49\cdot10^{-4}$ $v_y = 0$	$v_x = 3.88\cdot10^{-4}$ $v_y = -3.88\cdot10^{-4}$
Particle Diameter (m)	$2\cdot10^{-6}$ $7\cdot10^{-6}$ $15\cdot10^{-6}$ $25\cdot10^{-6}$	- $7\cdot10^{-6}$ - -	- $7\cdot10^{-6}$ - -	- $7\cdot10^{-6}$ - -	- $7\cdot10^{-6}$ - -
Specific Gravity	1.1 1.5	1.1 -	1.1 -	1.1 -	1.1 -

Table 5. Calculated collector efficiencies for different particle sizes at an approach velocity of $-5.49\cdot10^{-4}$ m/sec in the $-y$ -direction. The particle specific gravity is 1.1.

Particle Diameter (m)	Collector Efficiency (%)
$2\cdot10^{-6}$	5.1
$7\cdot10^{-6}$	55.6
$15\cdot10^{-6}$	56.0
$25\cdot10^{-6}$	68.0

Table 6. Calculated collector efficiencies for $25\cdot10^{-6}$ m diameter particles at an approach velocity of $-5.49\cdot10^{-4}$ m/sec in the $-y$ -direction. The particle specific gravity is 1.1 or 1.5.

Specific Gravity	Collector Efficiency (%)
1.1	68.0
1.5	81.1

Table 7. Calculated collector efficiencies for different approach velocities for the particles of $7 \cdot 10^{-6}$ m diameter.

Approach Velocity (m/sec)	Collector Efficiency (%)
$v_x = 0, v_y = -5.49 \cdot 10^{-4}$	55.6
$v_x = 0, v_y = -2.76 \cdot 10^{-4}$	53.5
$v_x = 0, v_y = -1.38 \cdot 10^{-4}$	43.7
$v_x = 5.49 \cdot 10^{-4}, v_y = 0$	46.9
$v_x = 3.88 \cdot 10^{-4}, v_y = -3.88 \cdot 10^{-4}$	44.3

Technology Transfer

NONE

Peer-Reviewed Publications

NONE

Awards/Honors Received

NONE

Army Laboratory Visits

June 2011